JM PAPERS

Stability analysis of a chemotaxis–convection–diffusion coupling system with the roles of deformed free surface and surface tension

S. Chakraborty[1] **and T.W.-H. Sheu**[1,2,†]

[1]Center for Advanced Study in Theoretical Sciences, National Taiwan University, No. 1, Sec. 4, Roosevelt Road, Taipei 10617, Taiwan, R.O.C.

[2]Department of Engineering Science and Ocean Engineering, National Taiwan University, No. 1, Sec. 4, Roosevelt Road, Taipei 10617, Taiwan, R.O.C.

We consider a three-dimensional chemotaxis–convection–diffusion coupled system with the effect of surface tension at the deformed free surface. The novelty of this research is to explore the impact of surface tension on bioconvection. Our aim is to determine the nature of the instability at the onset of bioconvection in a chemotaxis–convection–diffusion system involving surface tension by performing a detailed linear stability analysis of steady-state cell and oxygen concentration distributions. The influence of the surface tension on the accumulated chemotaxis cells at the deformed free surface is studied analytically to illustrate its effect on the stability of the system. The Froude number, Fr_τ, and capillary number, Ca_τ, are two additional parameters introduced here. A detailed parametric study is undertaken to investigate the roles of the critical Rayleigh number, $Ra_{\tau c}$, as well as Fr_τ and Ca_τ, in the chemotaxis system. Linear stability results revealed that an increasing value of Ra_τ would stabilize the chemotaxis system. At a higher value of Fr_τ, the motion of the cells is faster towards the free surface, and as the surface tension force increases, less accumulated cells are found at the free surface. A cluster of the cells can be observed mostly at the trough rather than on the crest of the wave profile. While experimental results for the present model are not yet available, the results of the linear stability analysis provide useful information about the system's stability.

Key words: bioconvection, buoyancy-driven instability

† Email address for correspondence: twhsheu@ntu.edu.tw

1. Introduction

Chemotaxis refers to the motion of chemical attractant cells or organisms in response to a chemical stimulus (Brenner, Levitov & Budrene 1998). The mathematical model of this kind of cell mobility was first derived by Patlak (1953) and Keller & Segel (1971). More specifically, Patlak (1953) derived a mathematical model for particle movement, whereas Keller & Segel (1971) were the first to derive a mathematical model for the real living cell movement. In a suspension of chemotaxis cells (e.g. *Bacillus subtilis*) in a container open to the air, complex bioconvection patterns are formed. These patterns appear because the slightly dense diluted cell consumes oxygen, swims towards the higher concentration of oxygen (i.e. upwards) and accumulates close to the free surface. This phenomenon triggers a density change in the suspension, and Rayleigh–Taylor-type instabilities occur. There are two somewhat unique cases: a 'shallow' and a 'deep' chamber. In a shallow chamber, cells can swim actively due to the presence of a high-enough oxygen concentration throughout the chamber, whereas in a deep chamber, the oxygen concentration starts to decrease towards the bottom of the chamber, away from the free surface. Therefore, the chamber can be divided into active and inactive regions. Bacteria consume oxygen and then freely move to the active region, the inactive region forms at the bottom of the chamber, and the cells in it become less active due to the lack of oxygen. Experiments with shallow chambers have shown the formation of various complex, irregular patterns (Hill & Pedley 2005; Bestehorn 2009). Experiments with a very shallow or tilted chamber have shown no pattern formation (Ko & Chase 1973; Pedley & Kessler 1992; Comer 2007). However, experiments with a deep chamber have shown regular and clear hexagonal bioconvection patterns, which turn more complex as the depth increases (Bees 1998). Due to its significant role in medical, industrial and geophysical areas, many research groups have devoted their efforts to understanding the dynamics of cell motility in suspension. The chemotaxis phenomenon can be successfully modelled by coupling the two convection–diffusion types of equations governing the cell and oxygen concentrations with the Navier–Stokes equations involving the Boussinesq approximation. Previously published mathematical models were derived only for the case with a flat free surface to investigate such phenomena (Kessler *et al.* 1994; Hillesdon, Pedley & Kessler 1995; Hillesdon & Pedley 1996; Metcalfe & Pedley 1998). Hill & Pedley (2005) reviewed the different mechanisms of up-swimming microorganisms and bioconvection. Chemotaxis–convection–diffusion is a particular type of bioconvection. The coupling phenomenon of chemotaxis, diffusion and convection has been illustrated in experiments of cell suspension by Hillesdon & Pedley (1996) and Hillesdon *et al.* (1995). The same phenomenon was successfully illustrated in numerical simulations by Chertock *et al.* (2012), Lee & Kim (2015) and Deleuze *et al.* (2016). It would be more interesting to study all these phenomena for the distorted free surface with the impact of surface tension as this is relevant to many natural settings.

The pattern formation of microorganisms has been studied theoretically, experimentally and numerically, with the main focus on the blow-up phenomena in a finite time either for a flat free surface or for rigid top and bottom surfaces. Avramenko & Kuznetsov (2010) performed a linear stability analysis of both rigid top and open flat free surfaces and obtained a correlation between the critical value of the bioconvection Rayleigh number and the traditional 'thermal' Rayleigh number by heating the fluid flow from below, whereas Kuznetsov (2005) studied the same phenomena under an inclined temperature gradient. Both studies proved that the flow system becomes more unstable when the fluid is heated from below.

Plume formation and its stabilization result from the balance between the chemotaxis, diffusion and convection of cells. It is a known fact that chemotaxis brings instability

to the nonlinear system and leads to aggregation; despite this fact, all previous stability analyses of the chemotaxis system were performed for the flat free surface only (Hill, Pedley & Kessler 1989; Hillesdon 1994; Hillesdon *et al.* 1995; Hillesdon & Pedley 1996; Metcalfe & Pedley 2001; Hill & Pedley 2005; Kuznetsov 2005; Avramenko & Kuznetsov 2010). Kowalczyk, Gamba & Preziosi (2004) performed a detailed linear stability analysis of two different models to check their potentials to form plumes on a homogeneous cell solution. However, Hillesdon & Pedley (1996) showed that the condition for linear instability of the chemotaxis–convection–diffusion system depends on the taxis Rayleigh number Ra_τ. Notably, previously published linear stability analysis results aid us in understanding the chemotaxis phenomenon at the onset of bioconvection. Moreover, nonlinear studies provide detailed information about the formation of complex bioconvection patterns/plumes and their respective stability in the system. Metcalfe & Pedley (1998) and Ma *et al.* (2016) performed weakly nonlinear stability analyses to investigate the stability of the different patterns forming in the chemotaxis system. Tuval *et al.* (2005) showed that the hydrodynamic vortices formed by convection strengthen the circulation of fluid and enhance the intake of oxygen into the solvent. Duan, Lorz & Markowich (2010) and Liu & Lorz (2011) proved the global existence of the chemotaxis–Stokes system under small and large initial cell population densities, respectively. Following this, Chertock *et al.* (2012) numerically studied plume formation in the system for the flat free surface and revealed that the number and shape of the plumes can be controlled by the initial cell population density.

Metcalfe & Pedley (2001) derived both two-dimensional and three-dimensional mathematical models for only the active region of a deep chamber where the cells are active. Their study showed that the system is unstable near the flat free surface. They also studied the phenomenon of the formation of falling plumes of fluid with high density cells. Performing stability analysis in a two-dimensional model is sufficient to obtain information about the nature of the instability at the onset of bioconvection. However, this is not enough to obtain detailed information about the cell dynamics in the nonlinear regime. Thus, performing nonlinear stability analysis of a three-dimensional model is essential. Through weakly nonlinear stability analysis, the phenomenon of the formation of patterns/plumes with its nature of stability and nonlinear cell dynamics can be studied in detail. Hill & Pedley (2005) considered only a shallow chamber to study the swimming behaviour of microorganisms, which involves nonlinear analysis of the patterns. Moreover, the stability analysis in both linear and nonlinear regimes was performed and discussed in detail by Metcalfe & Pedley (1998). Hillesdon *et al.* (1995) formulated a three-dimensional model for both shallow and deep chambers and studied the formation of plumes. Their numerical results showed good qualitative agreement with experimental results. Hill *et al.* (1989) carried out linear stability analyses on the flat interfaces of a shallow and a finite depth chamber. Their investigations showed that the suspension becomes more unstable as the depth of the chamber increases. Pedley, Hill & Kessler (1988) performed a linear stability analysis of an infinite uniform suspension. Their results were verified again by Hill *et al.* (1989).

To study the dynamics of the chemotaxis–convection–diffusion system, the stability analysis must be performed in both linear and nonlinear regimes. Hillesdon & Pedley (1996) followed the same trail as Hillesdon *et al.* (1995) did in their study on stability analysis and performed a linear stability analysis for both shallow and deep chambers to understand the nature of stability at the onset of bioconvection. In a shallow layer, there is a large amount of oxygen, while in a deep layer, there is a region far from the free surface where oxygen and, consequently, the cell concentration gradients are zero.

This linear stability analysis was followed by a weakly nonlinear stability analysis by Metcalfe & Pedley (1998) to predict the patterns when the suspension is just deep enough for patterns to form. They drew the bifurcation diagram to exhibit the behaviour of the system. However, Hill & Pedley (2005) performed a nonlinear stability analysis of pattern formation, and their study included the dispersion in shear flows along with the swimming behaviour of algal cells. It would be interesting to conduct the linear and nonlinear stability analyses of the chemotaxis–convection–diffusion system with deformed free surface and with the effect of surface tension.

Chakraborty *et al.* (2018) performed a linear stability analysis of the two-dimensional distorted free surface of a chemotaxis–convection–diffusion system in a shallow chamber to investigate the formation of patterns at the onset of instability. However, the effect of the surface tension on the interfacial flow in a shallow chamber was neglected. It has been seen that the small but finite amplitude perturbations of the free surface are sufficient to trigger instability. Recently, Ivančić, Sheu & Solovchuk (2019) published their work on the effect of surface tension, σ, which is a function of cell concentration, n. They solved the problem numerically by modifying the presently available model to render a more realistic one in both two and three dimensions, and they noted that the higher concentration of cells on the free surface decreases the effect of the surface tension of the fluid, which may have a significant impact on the onset of instability. It would be interesting to study the impact of surface tension on cell concentration and *vice versa*.

It was found in the literature that surface tension plays an important role in a thin film flow problem. It has a significant influence on the holding of the wave profile's shape. The occurrence of capillary ripples in a flow problem is mainly due to the presence of surface tension. This is why we were motivated to take into account the surface tension effect to describe the dynamics of the chemotaxis–convection–diffusion coupling system in a shallow chamber with a deformed free surface. A stability analysis of a three-dimensional chemotaxis system in a shallow chamber that considers the effect of surface tension at the deformed free surface has not been attempted yet. In this paper, we consider a homogeneous suspension with a deformed free surface in a shallow rectangular chamber. The novel aspects of the present work are that the free surface is allowed to deform, the surface tension effect is taken into account along with consideration of the free surface stress boundary condition of the chemotaxis system. Our aim is to explore the linear and nonlinear stability analyses of the chemotaxis–convection–diffusion system.

Most of the previously published studies were devoted to the chemotaxis system with the flat free surface and successfully explained the formation of patterns and the dynamics of falling plumes. However, the free surface is normally deformable in natural conditions. To the best of the authors' knowledge, the linear and nonlinear stability analyses of the chemotaxis-convection-diffusion system for deformed free surface have not been performed yet. Most of the previously performed studies were devoted to the shallow chamber case. However, there are still many things worth exploring with regard to the deep chamber case. In the natural scenario, the chemotaxis system is complex in nature, and for this reason, nonlinear stability analysis needs to be performed. It is obvious that the presence of surface tension and normal, tangential stress boundary conditions will have a phenomenal impact on the pattern formation and the behaviour of the system. Therefore, we felt stimulated to perform the present study. We have performed linear and weakly nonlinear (in an upcoming paper) stability analyses at the onset of instability to study the dynamics of the formation of the patterns while considering the effect of the surface tension. It is a known fact that linear stability analysis provides only a basic idea about the formation of patterns. It cannot explain well the amplitude, types and significant physical role of pattern formation that results from cross-diffusion in the chemotaxis system.
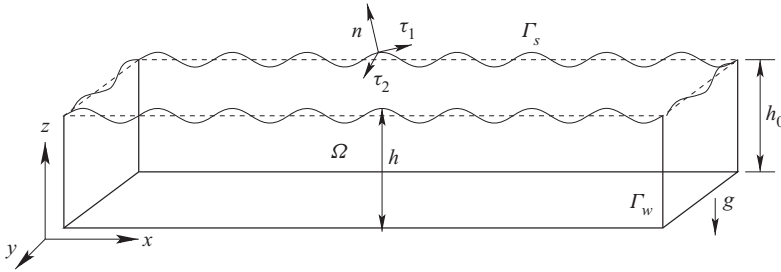
Figure 1. Schematic diagram of a three-dimensional chemotaxis system with liquid–air interface Γ_s, where the oxygen concentration is equal to that of air, not crossed by cell. No-slip boundary condition is imposed at the container walls Γ_w.

Thus, conducting weakly nonlinear stability analysis becomes necessary. Conducting nonlinear stability analysis would help us predict the characteristics of the patterns formed in the system. Besides, it would be really interesting to investigate the formation of these patterns under the influence of surface tension at the deformed free surface. However, to keep the present paper at a reasonable length, we provide only a detailed study of the linear stability analysis of the chemotaxis system. A complete study of the weakly nonlinear stability analysis will be presented in the next article. A comparison and detailed discussion of the numerical simulation results underlying the bifurcation theory will be included in an upcoming article.

The paper is organized as follows: the mathematical formulation of the chemotaxis–convection–diffusion system is presented and the steady-state solution is described in § 2. The linear stability analysis is performed and its analytical solutions are presented in § 3. The stability analysis results are discussed in § 4. Finally, some conclusions are summarized and recommendations for future works are provided in § 5.

2. Mathematical model

A three-dimensional shallow rectangular chamber containing an incompressible fluid with deformed free surface is considered. For the mathematical description of the three-dimensional chamber, we use a Cartesian coordinate system (x, y, z), referring to the streamwise, spanwise and cross-wise coordinates, respectively. The top of the chamber is open to the air, and the motion of the fluid flow in a rectangular chamber is subjected to the tangential stress condition prescribed on the free surface, $z = h(x, y, t)$. The bottom and the sidewalls are rigid and impermeable to cells and oxygen (see figure 1).

Under the full Boussinesq approximation, the dimensional form of the governing equations for the chemotaxis–convection–diffusion elliptic–parabolic system of equations for an incompressible fluid flow is as follows:

$$\nabla \cdot \boldsymbol{u} = 0, \qquad (2.1a)$$

$$\rho \left(\boldsymbol{u}_t + \boldsymbol{u} \cdot \nabla \boldsymbol{u} \right) + \nabla p - \mu \nabla^2 \boldsymbol{u} = -\rho g \boldsymbol{k} - n V_b g (\rho_b - \rho) \boldsymbol{k}, \qquad (2.1b)$$

$$n_t + \nabla \cdot [\boldsymbol{u} n - D_b \nabla n + S_{dim} r(c) n \nabla c] = 0, \qquad (2.1c)$$

$$c_t + \nabla \cdot (\boldsymbol{u} c - D_O \nabla c) = -n \kappa r(c), \qquad (2.1d)$$

where $\boldsymbol{u} = (u, v, w)$ denotes the flow velocity in the (x, y, z)-direction; p denotes the hydrostatic pressure, ρ and μ the fluid density and viscosity; g denotes the gravitational acceleration, n the number of cells per unit area, V_b and ρ_b the volume and volumetric

mass density of a cell, respectively, and c the oxygen concentration. The source term $V_b g(\rho_b - \rho) \boldsymbol{k}$ stands for the buoyancy force exerted by a cell on the liquid in the vertical direction, where $\boldsymbol{k}$ denotes the unit vector. The parameter S_{dim} in (2.1c) is the dimensional chemotaxis sensitivity (the movement of cell towards higher concentration depends on the chemotaxis sensitivity, S_{dim}); D_b and D_O are the cell and oxygen diffusivities. In (2.1d), κ is the rate of consumption of oxygen by bacterium. Bacteria are considered to be slightly denser than water such that $\rho_b > \rho$, where cells are supposed to swim in the water during the consumption of oxygen. Therefore, we have assumed $(\rho_b - \rho)/\rho \ll 1$ and $nV_b \ll 1$. The oxygen consumption is proportional to the cell population density n. The cell (n) and oxygen (c) concentrations are advected by the liquid flow. When the concentration of oxygen is lower than a threshold value, the cells become stable or inactive, i.e. they neither consume oxygen nor swim towards the region with higher oxygen concentration. This procedure is indicated by a non-dimensional cutoff function, $r(c)$, which is defined by the step function

$$r(c) = \begin{cases} 1, & \text{if } c > c^* \\ 0, & \text{if } c \leqslant c^* \end{cases} \tag{2.2}$$

where $c^* = 0.3$ was derived by experiments (Hillesdon *et al.* 1995; Hillesdon & Pedley 1996) (see supplementary material available at https://doi.org/10.1017/jfm.2021.508 for concise nomenclature).

The set of equations (2.1a)–(2.1d) is closed with the boundary conditions and will be solved in a three-dimensional rectangular container (Ω). The dynamic boundary conditions applied at the interface ($z = h(x, y, t)$) are

$$\boldsymbol{n} \cdot \bar{\tau} \cdot \boldsymbol{n} = -(\nabla \cdot \boldsymbol{n})\,\sigma, \tag{2.3a}$$

$$\boldsymbol{t}_1 \cdot \bar{\tau} \cdot \boldsymbol{n} = 0, \tag{2.3b}$$

$$\boldsymbol{t}_2 \cdot \bar{\tau} \cdot \boldsymbol{n} = 0. \tag{2.3c}$$

The stresses along the tangential and normal directions are balanced at the interface, $z = h(x, y, t)$. The boundary conditions for cell and oxygen concentrations at the interface are

$$S_{dim} n r(c) \nabla c \cdot \boldsymbol{n} = D_b \nabla n \cdot \boldsymbol{n}, \tag{2.3d}$$

$$c = c_{air}. \tag{2.3e}$$

The kinematic boundary condition is

$$h_t = w - uh_x - vh_y, \tag{2.3f}$$

where $\bar{\tau}$ is the stress tensor for the liquid, $\boldsymbol{n}(= (-h_x, -h_y, 1)/N)$ and $\boldsymbol{t}_1(= (1, 0, h_x)/\sqrt{1 + h_x^2})$ and $\boldsymbol{t}_2(= (0, 1, h_y)/\sqrt{1 + h_y^2})$ are the unit outward normal and tangential vectors on the interface and $N = \sqrt{1 + h_x^2 + h_y^2}$. A no-slip boundary condition is applied on the container walls (Γ_w); the fluxes of cell and oxygen are equal to zero

$$u = 0, \quad v = 0, \quad w = 0, \quad \nabla n \cdot \boldsymbol{n} = 0, \quad \nabla c \cdot \boldsymbol{n} = 0. \tag{2.3g}$$

The characteristic cell density is defined as the average of the initial cell population

$$\overline{n_0} = \frac{1}{|\Omega|} \int_\Omega n_0(x, y, t)\,\mathrm{d}x. \tag{2.4}$$

By the choice of this characteristic cell density, the total number of cells can be measured easily in each simulation under different initial distributions of cells.

Equations (2.1)–(2.3) can be expressed in terms of their dimensionless forms by using the following variables:

$$x = Lx', \quad y = Ly', \quad z = h_0 z', \quad h = h_0 h', \quad n = \overline{n}_0 n', \quad c = c_{air} c',$$
$$t = \frac{h_0^2}{\varepsilon D_b} t', \quad p = \frac{\mu D_b}{\varepsilon h_0^2} p', \quad u = \frac{D_b}{h_0} u', \quad v = \frac{D_b}{h_0} v' \quad w = \frac{\varepsilon D_b}{h_0} w',$$
$$(2.5a\text{–}k)$$

where h_0 and L are the characteristic length scales in the vertical and horizontal directions, respectively, $\varepsilon = h_0/L \ll 1$ is an aspect ratio. Finally, after dropping the prime from the dimensionless quantities, the dimensionless Navier–Stokes equations for the incompressible fluid flow and the Keller–Segel equation for n and c can be read as

$$u_x + v_y + w_z = 0, \tag{2.6a}$$

$$\varepsilon(u_t + uu_x + vu_y + wu_z) + Pr_\tau p_x = Pr_\tau[\varepsilon^2(u_{xx} + u_{yy}) + u_{zz}], \tag{2.6b}$$

$$\varepsilon(v_t + uv_x + vv_y + wv_z) + Pr_\tau p_y = Pr_\tau[\varepsilon^2(v_{xx} + v_{yy}) + v_{zz}], \tag{2.6c}$$

$$\varepsilon^3(w_t + uw_x + vw_y + ww_z) + Pr_\tau p_z = \varepsilon^2 Pr_\tau[\varepsilon^2(w_{xx} + w_{yy}) + w_{zz}] - \varepsilon Fr_\tau^{-2}$$
$$-\varepsilon Pr_\tau Ra_\tau n, \tag{2.6d}$$

$$\varepsilon(n_t + un_x + vn_y + wn_z) = [\varepsilon^2(n_{xx} + n_{yy}) + n_{zz}] - S_\tau r(c)(n[\varepsilon^2(c_{xx} + c_{yy}) + c_{zz}]$$
$$+ [\varepsilon^2(c_x n_x + c_y n_y) + c_z n_z]), \tag{2.6e}$$

$$\varepsilon(c_t + uc_x + vc_y + wc_z) + H_\tau r(c)n = Le_\tau[\varepsilon^2(c_{xx} + c_{yy}) + c_{zz}]. \tag{2.6f}$$

The above set of dimensionless governing equations is subject to the dimensionless boundary conditions prescribed on the deformed free surface $z = h(x, y, t)$

$$-p + \frac{2\varepsilon^2[\varepsilon^2(u_x h_x^2 + (u_y + v_x)h_x h_y + v_y h_y^2) - (u_z + \varepsilon^2 w_x)h_x - (v_z + \varepsilon^2 w_y)h_y + w_z]}{[1 + \varepsilon^2(h_x^2 + h_y^2)]}$$
$$= \frac{\varepsilon^3[(1 + \varepsilon^2 h_x^2)h_{yy} - 2\varepsilon^2 h_x h_y h_{xy} + (1 + \varepsilon^2 h_y^2)h_{xx}]}{Ca_\tau[1 + \varepsilon^2(h_x^2 + h_y^2)]^{3/2}}, \tag{2.7a}$$

$$(1 - \varepsilon^2 h_x^2)(u_z + \varepsilon^2 w_x) + 2\varepsilon^2(w_z - u_x)h_x - \varepsilon^2(u_y + v_x)h_y - \varepsilon^2(v_z + \varepsilon^2 w_y)h_x h_y = 0, \tag{2.7b}$$

$$(1 - \varepsilon^2 h_y^2)(v_z + \varepsilon^2 w_y) + 2\varepsilon^2(w_z - v_y)h_y - \varepsilon^2(u_y + v_x)h_x - \varepsilon^2(u_z + \varepsilon^2 w_x)h_x h_y = 0, \tag{2.7c}$$

$$S_\tau r(c)n[c_z - \varepsilon^2(c_x h_x + c_y h_y)] - [n_z - \varepsilon^2(n_x h_x + n_y h_y)] = 0, \tag{2.7d}$$

$$c = 1. \tag{2.7e}$$

On the other boundaries, we prescribe

$$u = 0, \quad v = 0, \quad w = 0, \tag{2.7f}$$

$$n_z = \varepsilon^2(n_x h_x + n_y h_y), \tag{2.7g}$$

$$c_z = \varepsilon^2(c_x h_x + c_y h_y). \tag{2.7h}$$

The kinematic boundary condition is

$$h_t + uh_x + vh_y = w. \tag{2.7i}$$

The dimensionless parameters are defined as

$$Pr_\tau = \frac{\nu}{D_b}, \quad Ra_\tau = \frac{gV_b\overline{n_0}(\rho_b - \rho)h_0^3}{D_b\mu}, \quad Fr_\tau = \frac{D_b}{\sqrt{gh_0^3}}, \quad Ca_\tau = \frac{\mu D_b}{\sigma h_0},$$

$$S_\tau = \frac{S_{dim}c_{air}}{D_b}, \quad H_\tau = \frac{\kappa\overline{n_0}h_0^2}{c_{air}D_b}, \quad Le_\tau = \frac{D_O}{D_b}. \qquad (2.8)$$

In the above equation, Pr_τ is the taxis Prandtl number, Ra_τ the taxis Rayleigh number (buoyancy-driven flow), Fr_τ the taxis Froude number, Ca_τ the taxis capillary number, S_τ the dimensionless chemotaxis sensitivity, H_τ the chemotaxis head and Le_τ the taxis Lewis number. The chemotaxis head represents the consumption of the chemo-attractant by the cell. The chemotaxis system is characterized by chemotaxis sensitivity (S_τ) and head (H_τ). It can be seen from (2.8) that only Ra_τ and H_τ depend on the characteristic length h_0 and the characteristic cell density $\overline{n_0}$. In summary, the hydrodynamic and chemotaxis transport equations currently under investigation are characterized by the above-mentioned seven non-dimensional parameters.

The present dimensionless parameters, such as Pr_τ, Ra_τ, Le_τ, S_τ and H_τ, are different from the parameters defined by Hillesdon & Pedley (1996). For better readability, the differences are stated as follows: $S_\tau \sim \gamma_{HP}$, $H_\tau/Le_\tau \sim \beta_{HP}$, $Le_\tau \sim \delta_{HP}$, $Pr_\tau \sim Sc_{HP}$ and $Ra_\tau \sim \Gamma_{HP}$, where the subscript HP refers to Hillesdon & Pedley (1996). Other dimensionless parameters in the present chemotaxis system are Ca_τ, which indicates the situation when a flow system comes into play due to the surface tension contribution, and Fr_τ, which exhibits the influence of gravity on cell diffusion.

2.1. *Steady-state solutions*

In steady-state flow, the fluid properties of the system do not change over time. The pressure, velocity and cell and oxygen concentrations will vary in the z-direction only. The solution for $p(z)$ is obtained as follows by integrating (2.6d) with the boundary condition (2.7a)

$$p(z) = \frac{\varepsilon}{Pr_\tau Fr_\tau^2}(1 - z). \qquad (2.9)$$

The solutions for $n(z)$ and $c(z)$ are obtained as follows:

$$c(z) = 1 - \frac{2}{S_\tau}\ln\left(\frac{\cos\left(\frac{S_\tau}{2}A_1 z\right)}{\cos\left(\frac{S_\tau}{2}A_1\right)}\right), \qquad (2.10a)$$

$$n(z) = \frac{S_\tau}{2}\frac{Le_\tau A_1^2}{H_\tau}\sec^2\left(\frac{S_\tau}{2}A_1 z\right), \qquad (2.10b)$$

where the unknown constant A_1 is determined from the transcendental equation given by Hillesdon & Pedley (1996)

$$\tan\left(\frac{S_\tau}{2}A_1\right) = \frac{H_\tau}{Le_\tau}\frac{1}{A_1}. \qquad (2.11)$$

Detailed derivations of steady-state solutions have been presented in previous publications (Hillesdon *et al.* 1995; Hillesdon & Pedley 1996; Chakraborty *et al.* 2018). Expansion of

the above equation yields a value of A_1 of the order of $O(H_\tau/Le_\tau)$. By substituting the value of A_1 into (2.10), we get the steady-state concentrations for cell and oxygen. The expansion of (2.11) is possible only when $A_1 \tan((S_\tau/2)A_1) = H_\tau/Le_\tau \ll 1$. It is necessary to expand the steady-state solutions (2.10) and (2.11) in powers of H_τ/Le_τ. The expansion for A_1 in (2.11), (2.10a) and (2.10b) gives, respectively,

$$A_1 = \left(\frac{2H_\tau}{S_\tau Le_\tau}\right)^{1/2} \left(1 - \frac{S_\tau}{12}\frac{H_\tau}{Le_\tau} + \frac{7S_\tau^2}{288}\frac{H_\tau^2}{Le_\tau^2} + O\left(\frac{H_\tau}{Le_\tau}\right)^3\right), \tag{2.12}$$

$$c = 1 + \frac{1}{2}(z^2 - 1)\frac{H_\tau}{Le_\tau} + \frac{S_\tau}{24}(z^2 - 1)^2\frac{H_\tau^2}{Le_\tau^2} + O\left(\frac{H_\tau}{Le_\tau}\right)^3, \tag{2.13}$$

$$n = 1 + \frac{S_\tau}{6}(3z^2 - 1)\frac{H_\tau}{Le_\tau} + \frac{S_\tau^2}{18}(1 - 3z^2 + 3z^4)\frac{H_\tau^2}{Le_\tau^2} + O\left(\frac{H_\tau}{Le_\tau}\right)^3. \tag{2.14}$$

It should be noted here that this shallow chamber instability problem depends on S_τ, H_τ and Le_τ and $Le_\tau \gg H_\tau$. From (2.12)–(2.13), we can also see that $c(z)$ and $n(z)$ can be written as functions of the two variables z and $S_\tau H_\tau/Le_\tau$. Note that the expressions for the steady-state solutions of the cell and oxygen concentrations in the present system are different from those mentioned in the works of Hillesdon (1994), Hillesdon & Pedley (1996) and Metcalfe & Pedley (1998) (steady-state profiles for a shallow chamber are independent of δ_{HP} and only vary with $\gamma_{HP}\beta_{HP}$).

3. Linear stability analysis

In this study, the aim behind conducting linear stability analysis is to investigate the onset of buoyancy-driven instability. The instability starts appearing if the Rayleigh number, which is the ratio of the buoyancy to viscous forces, reaches a critical value. In this section, we seek the critical Rayleigh number, which is the function of the physical parameters of the system. We first linearize the governing equations in (2.6) by adding small perturbations to the steady-state solutions. Then, the resulting equations are solved for perturbations with a wavenumber k, which corresponds to the dimensionless wavelength $\lambda = 2\pi/k$.

Here, we perturb the following field variables with respect to their respective basic state solutions:

$$\boldsymbol{u}(\boldsymbol{x}, t) = \epsilon\tilde{\boldsymbol{u}}(\boldsymbol{x}, t), \tag{3.1a}$$

$$p(\boldsymbol{x}, t) = p(z) + \epsilon\tilde{p}(\boldsymbol{x}, t), \tag{3.1b}$$

$$n(\boldsymbol{x}, t) = n(z) + \epsilon\tilde{n}(\boldsymbol{x}, t), \tag{3.1c}$$

$$c(\boldsymbol{x}, t) = c(z) + \epsilon\tilde{c}(\boldsymbol{x}, t), \tag{3.1d}$$

$$h(\boldsymbol{x}, t) = 1 + \epsilon\tilde{\eta}(\boldsymbol{x}, t), \tag{3.1e}$$

where the components of $\tilde{\boldsymbol{u}}$ are $(\tilde{u}, \tilde{v}, \tilde{w})$ and $\boldsymbol{x}$ denotes (x, y, z). After substituting (3.1) into the dimensionless governing equations (2.6) along with the dimensionless boundary conditions (2.7) and eliminating $\tilde{u}$, $\tilde{v}$ and $\tilde{p}$, the resulting equations can be expressed in terms of $\tilde{w}$, $\tilde{n}$, $\tilde{c}$ and $\tilde{\eta}$ only. Then, the solutions are sought in the form of normal modes

$$[\tilde{w}, \tilde{n}, \tilde{c}, \tilde{\eta}] = [W(z), N(z), C(z), \eta]\exp(\mathrm{i}(k_x x + k_y y) - \omega t). \tag{3.2}$$

923 A14-9

Introducing (3.2) into the perturbation expressions given in (3.1*a*) and (3.1*c*)–(3.1*e*), the resulting system of equations renders

$$\left[\frac{d^2}{dz^2} - \left(\frac{\varepsilon\omega}{Pr_\tau} + \varepsilon^2 k^2 \right) \right] \left(\frac{d^2}{dz^2} - \varepsilon^2 k^2 \right) W + \varepsilon k^2 Ra_\tau N = 0, \tag{3.3a}$$

$$\frac{d^2 N}{dz^2} - S_\tau \frac{dc}{dz} \frac{dN}{dz} - \left(\varepsilon^2 k^2 - \varepsilon\omega + S_\tau \frac{d^2 c}{dz^2} + n(z) \frac{H_\tau S_\tau}{Le_\tau} \right) N$$

$$= \varepsilon \frac{dn}{dz} W + S_\tau \left(\frac{\varepsilon n(z)}{Le_\tau} \frac{dc}{dz} W + \frac{dn}{dz} \frac{dC}{dz} - \frac{\varepsilon\omega n(z)}{Le_\tau} C \right), \tag{3.3b}$$

$$\frac{d^2 C}{dz^2} - \left(\frac{\varepsilon\omega}{Le_\tau} + \varepsilon^2 k^2 \right) C - \frac{\varepsilon}{Le_\tau} \frac{dc}{dz} W - \frac{H_\tau}{Le_\tau} N = 0, \tag{3.3c}$$

where $k = \sqrt{k_x^2 + k_y^2}$, k_x and k_y are the wavenumbers of the disturbance in the x- and y-directions, and ω is the complex angular frequency, which has the complex wave velocity $c = \omega/k$. Seeking of the solutions to the above system of equations (3.3) is subject to the boundary conditions prescribed at the interface and at the other boundaries

$$2\varepsilon^2 \omega Ca_\tau \frac{dW(1)}{dz} + \varepsilon \left(\varepsilon^2 k^2 + \frac{Ca_\tau}{Pr_\tau Fr_\tau^2} \right) W(1) = 0, \tag{3.3d}$$

$$\frac{d^3 W(1)}{dz^3} + \varepsilon^2 k^2 \frac{dW(1)}{dz} = 0, \tag{3.3e}$$

$$\frac{dN(1)}{dz} - S_\tau \frac{dc(1)}{dz} N(1) - S_\tau n \frac{dC(1)}{dz}$$

$$= \frac{1}{\omega} \frac{d^2 n(1)}{dz^2} W(1) - \frac{S_\tau}{\omega} \left(n \frac{d^2 c(1)}{dz^2} + \frac{dc(1)}{dz} \frac{dn(1)}{dz} \right) W(1), \tag{3.3f}$$

$$C(1) = 0, \tag{3.3g}$$

$$W(0) = 0, \quad \frac{dW(0)}{dz} = 0, \quad \frac{dN(0)}{dz} = 0, \quad \frac{dC(0)}{dz} = 0. \tag{3.3h}$$

No-slip boundary condition is directly implemented in the numerical simulations. Use of periodic boundary conditions will be helpful in stability analysis. It should be mentioned that Ca_τ and Fr_τ have significant effects on the free surface of the chemotaxis flow system. To perform temporal stability analysis, we consider real wavenumber components k_x, k_y (the disturbance travels in the direction $\tan^{-1}(k_y/k_x)$), and the temporal growth rate is ω_i. If $\omega_i > 0$, the disturbance grows in time with the phase velocity ω_r/k. The real angular frequency is ω_r, while the phase velocities along the x, y axes are ω_r/k_x, ω_r/k_y, respectively (subscripts r and i denote the real and imaginary parts, respectively). The real angular frequency is related to the ordinary frequency and will be written in terms of a wave velocity c_r and a wavelength λ, i.e. $f = c_r/\lambda = c_r/(2\pi/k) = \omega_r/(2\pi)$ or $\omega_r = 2\pi f$.

When performing spatial stability analysis, we impose wavenumber components ω as real and seek k_x and k_y. The spatial growth rate is $-k_{x_i}$. If $k_{x_i} < 0$, the disturbance grows in space and the phase velocity is ω/k_{x_r}.

We solve the above system of equations shown in (3.3) using AUTO07P software (Doedel 2008). The spatial stability analysis (k complex and ω real) is performed starting from its analytical solution at $k = 0$.

3.1. *Analytical solutions*

We would like to express W, C and N in powers of $S_\tau H_\tau / Le_\tau$. Then, the leading term (and higher orders, if desired) will possibly be obtained in each of the series. For the sake of simplicity, we consider the case with a small wavenumber $k \sim (S_\tau H_\tau / Le_\tau)^{1/2}$, such that $k^2 = \tilde{k}^2 (S_\tau H_\tau / Le_\tau)$ is of order $O(1)$ (this is to keep the dimensional wavenumber fixed as $h \to 0$). The statement 'the higher-order derivative and the right-hand side must hold in (3.3a) at the leading order of W' is required to get a non-trivial solution. Then, the reduced equation takes the form

$$\left(\frac{d^2}{dz^2} - \frac{\varepsilon \omega}{Pr_\tau} \right) \frac{d^2 W}{dz^2} = -\varepsilon \tilde{k} \frac{S_\tau H_\tau}{Le_\tau} N Ra_\tau, \tag{3.4}$$

i.e. the viscous force, $d^4 W / dz^4$, balances the buoyancy force on the right-hand side, leaving aside the time dependence on ω. Without any loss of generality, we also specify that $N = 1$ at $z = 1$, and set $C = (H_\tau / Le_\tau) \bar{C}$. Now, we have the possibility of getting the leading orders of N and $\bar{C}$ in (3.3b) and (3.3c), which prospectively lead to the non-trivial solutions. Here, two cases can be considered: first, $Ra_\tau \sim O(1)$ and $\omega \sim O(S_\tau H_\tau / Le_\tau)$; second, $Ra_\tau \sim O(Le_\tau / S_\tau H_\tau)$ and $\omega \sim O(S_\tau H_\tau / Le_\tau)$ (for detail, see Hillesdon & Pedley 1996; Chakraborty *et al.* 2018). However, the solutions of the first case render a negative value of ω, indicating that the system is stable under all circumstances. For this reason, we choose the second case to perform the analysis where it is desirable to carry out expansions of the form

$$N(z) = \sum_{i=0}^{\infty} N_i(z) \left(\frac{S_\tau H_\tau}{Le_\tau} \right)^i, \quad \bar{C}(z) = \sum_{i=0}^{\infty} \bar{C}_i(z) \left(\frac{S_\tau H_\tau}{Le_\tau} \right)^i,$$

$$W(z) = \sum_{i=0}^{\infty} W_i(z) \left(\frac{S_\tau H_\tau}{Le_\tau} \right)^i,$$

and

$$\omega(\tilde{k}) = \sum_{i=1}^{\infty} \omega_i(\tilde{k}) \left(\frac{S_\tau H_\tau}{Le_\tau} \right)^i, \quad Ra_\tau(\tilde{k}) = \sum_{i=-1}^{\infty} Ra_{\tau_i}(\tilde{k}) \left(\frac{S_\tau H_\tau}{Le_\tau} \right)^i. \tag{3.5}$$

So, at the leading order, the governing equations become

$$\frac{d^4 W_0}{dz^4} = -\varepsilon \tilde{k}^2 N_0 Ra_{\tau -1}, \quad \frac{d^2 \bar{C}_0}{dz^2} = N_0, \quad \frac{d^2 N_0}{dz^2} = 0, \tag{3.6a–c}$$

with the boundary conditions

$$\frac{d^3 W_0(1)}{dz^3} = 0, \quad \frac{d^2 W_0(1)}{dz^2} = 0, \quad \bar{C}_0(1) = 0, \quad \frac{dN_0(1)}{dz} = 0,$$

$$\frac{dW_0(0)}{dz} = 0, \quad W_0(0) = 0, \quad \frac{dN_0(0)}{dz} = 0, \quad \frac{d\bar{C}_0(0)}{dz} = 0. \tag{3.7}$$

In this study, we have arbitrarily set $N_0 = 1$ at $z = 1$, and the corresponding solutions are

$$W_0(z) = -\frac{\tilde{k}^2 \varepsilon Ra_{\tau_{-1}}}{24} z^2 (z^2 - 4z + 6), \qquad (3.8a)$$

$$\bar{C}_0(z) = \tfrac{1}{2}(z^2 - 1), \qquad (3.8b)$$

$$N_0(z) = 1. \qquad (3.8c)$$

At the next order, the governing equations are

$$\left. \begin{aligned} \frac{d^4 W_1}{dz^4} &= \left(\frac{\varepsilon \omega_1}{Pr_\tau} + 2\tilde{k}^2 \varepsilon^2 \right) \frac{d^2 W_0}{dz^2} - \tilde{k}^2 \varepsilon \left(Ra_{\tau_0} N_0 + Ra_{\tau_{-1}} N_1 \right), \\ \frac{d^2 \bar{C}_1}{dz^2} &= N_1 + \tilde{k}^2 \varepsilon^2 \bar{C}_0, \\ \frac{d^2 N_1}{dz^2} &= (2 + \varepsilon \omega_1 + \tilde{k}^2 \varepsilon^2) N_0 + z \frac{dN_0}{dz} + z\varepsilon W_0, \end{aligned} \right\} \qquad (3.9)$$

with the boundary conditions

$$\left. \begin{aligned} \frac{d^3 W_1(1)}{dz^3} + \tilde{k}^2 \varepsilon^2 \frac{dW_0(1)}{dz} &= 0, \\ W_1(1) + 2\varepsilon \omega_1 Pr_\tau Fr_\tau^2 \frac{dW_0(1)}{dz} + \tilde{k}^2 \varepsilon^2 \frac{Pr_\tau Fr_\tau^2}{Ca_\tau} W_0(1) &= 0, \\ \frac{dN_1(1)}{dz} - \frac{d\bar{C}_0(1)}{dz} + \frac{\omega_2}{\omega_1} \frac{dN_0(1)}{dz} - N_0(1) &= 0, \quad \bar{C}_1(1) = 0, \\ \frac{dW_1(0)}{dz} = 0, \quad W_1(0) = 0, \quad \frac{dN_1(0)}{dz} = 0, \quad \frac{d\bar{C}_1(0)}{dz} = 0. \end{aligned} \right\} \qquad (3.10)$$

Then, we solve the above system of equations with the corresponding boundary conditions to get the solutions of W_1, $\bar{C}_1$ and N_1 at the first order. The solutions are given in Appendix A.

Similarly, we will solve the system of equations at the second order using the zeroth- and first-order solutions which are mentioned in Appendix A.

The first-order solution consists of functions of N_1, $\bar{C}_1$ and W_1, and we can obtain

$$\omega_1 = 0, \quad \text{or,} \quad \omega_1 = \tilde{k}^2 \varepsilon \left(\frac{7}{1440} Ra_{\tau-1} - 1 \right), \qquad (3.11a,b)$$

i.e. the instability is either stationary or non-oscillatory.

For the second-order solution, we find ω_2 as follows:

$$\omega_2 = \frac{\tilde{k}^2 \varepsilon (7Ra_{\tau-1} - 1440)(7!\tilde{k}^2 \varepsilon^2 Fr_\tau^2 Pr_\tau^2 + (37\tilde{k}^2 \varepsilon^2 - 784) Pr_\tau - 102\tilde{k}^2 \varepsilon^2)}{8!21 Pr_\tau}. \qquad (3.12)$$

It can be noticed from (3.11a,b) that the system is unstable to small wavenumber disturbances if $Ra_{\tau_{-1}} > (1440/7)$. The resultant instability indicates that the system under

923 A14-12

investigation is non-oscillatory. It would be interesting to study the marginal stability when $\omega_r = 0$ and calculate ω_i. Marginal stability ($\omega = 0$) occurs when

$$Ra_\tau(\tilde{k}) = \frac{1440}{7(S_\tau H_\tau / Le_\tau)} + O(1). \tag{3.13}$$

The correction of Ra_{τ_0} to the value of $Ra_\tau(\tilde{k})$ in (3.13) for marginal stability can now be found in terms of $Ra_{\tau_{-1}}$ and $\tilde{k}^2$ using (3.12).

4. Results and discussions

In the present paper, we have introduced two new physical dimensionless parameters, namely, the Froude number, Fr_τ, and the capillary number, Ca_τ, which are varied in the parametric study and discussed in detail. We have also independently varied other physical parameters such as Le_τ, S_τ, H_τ and ε, in the parametric study. The impact of these parameters on the chemotaxis–convection–diffusion system is addressed in the following sections. The results are discussed according to the variation of parameters. The following results are plotted using analytical solutions in § 3.1.

4.1. *Vary Le_τ; other parameters are fixed*

The steady-state profiles for a shallow chamber are dependent on Le_τ, H_τ and S_τ; however, in Hillesdon & Pedley (1996), these profiles are independent of δ_{HP} and vary only with $\gamma_{HP}\beta_{HP}$. It is also important to recall that they considered the vertical axis of the shallow chamber as $z = 1$ at bottom and $z = 0$ at the top, whereas we have taken the axis to be the vertical direction opposite to it, i.e. $z = 0$ at the bottom and $z = 1$ at the top boundary. We have changed the axes orientation of the model of Hillesdon & Pedley (1996) and presented their results in comparison with ours in figure 2. Since the steady-state solutions of cell and oxygen concentrations in Hillesdon & Pedley (1996) are independent of δ_{HP}, we have compared our steady-state results for $Le_\tau = 1$ and also varied the value of $Le_\tau = 5$ to study the impact of the diffusivity variations. The results for a variety of shallow chamber examples have been presented, in which they covered the whole steady-state density profiles ranging from $S_\tau H_\tau / Le_\tau \sim \gamma_{HP}\beta_{HP} = 0.8$ (nearly uniform) to $S_\tau H_\tau / Le_\tau \sim \gamma_{HP}\beta_{HP} = 300$ (highly dense at the top). It can be observed from the comparison that the concentration levels of both cells and oxygen are equally distributed. However, the variation of Le_τ shows that the movement of the cells becomes much faster as the diffusivity of oxygen increases. Figures 2(*a*) and 2(*b*) show the steady-state cell and oxygen concentration profiles, respectively, at the uniform stage, and figures 2(*c*) and 2(*d*) show the profiles at the top of the shallow chamber, where the cell concentration starts getting denser (i.e. at the top boundary). Cell mobility in the present study is comparatively rapid but in a less non-scattered manner compared with that in the study by Hillesdon & Pedley (1996). In fact, the cell concentration profile is found to be quite close to the oxygen distribution profile. It should be noted that the impact of the surface tension will be seen in the perturbed cell and oxygen concentration profiles in the linear stability analysis since the surface tension is non-zero at the free surface.

In § 2, we have mentioned that the five dimensionless parameters $Le_\tau, H_\tau, S_\tau, Pr_\tau$ and Ra_τ are slightly different from those Hillesdon & Pedley (1996) referred to. A few estimated parametric values from the linear stability analysis conducted in the present study are compared with the published results of Hillesdon & Pedley (1996) in table 1. The differences are apparent because the present study involves the values of Fr_τ and Ca_τ.
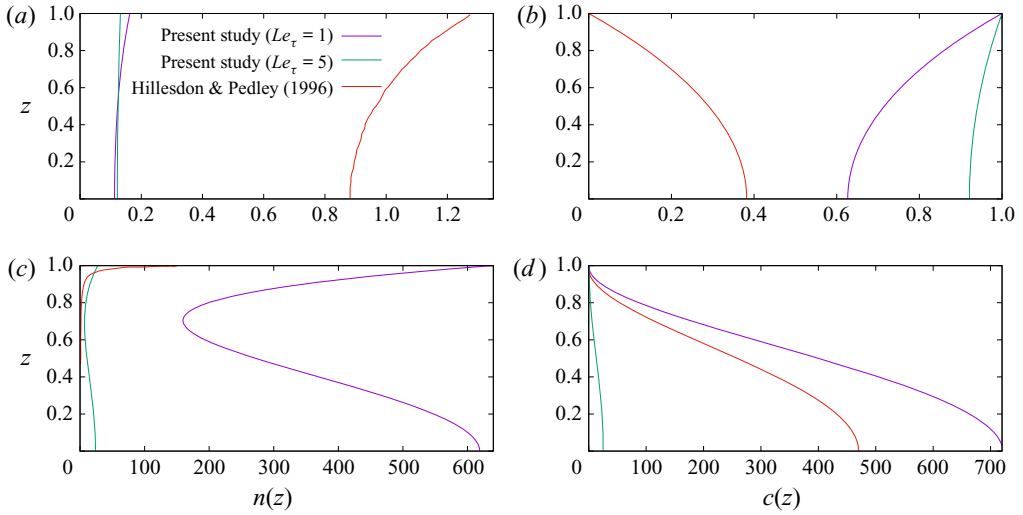
Figure 2. Steady-state cell and oxygen concentration profiles of Hillesdon & Pedley (1996) are plotted to make a comparison with those of the present study. The parameter values of $\gamma_{HP} \sim S_\tau = 1$ and $\beta_{HP} \sim H_\tau = 0.8$ in (a,b); and $\gamma_{HP} \sim S_\tau = 5$ and $\beta_{HP} \sim H_\tau = 60$ in (c,d), are taken into account.

Le_τ	$S_\tau H_\tau$	Γ_c-HP	k_c-HP	$Ra_{\tau c}$-Present	k_c-Present	ε	Fr_τ
1	0.05	1.02×10^4	1.37	15234.24	154.4	0.1	0.001
1	1	625	1.58	811.183	34.4	0.1	0.001
1	1	—	—	811.183	17.2	0.2	0.001
1	1	—	—	811.183	6.9	0.5	0.001
1	10	200	1.90	240.299	10.8	0.1	0.001
1	50	328	1.94	681.248	4.8	0.1	0.001
1	100	522	1.91	1300.81	3.3	0.1	0.001
10	10	241	1.29	811.183	34.4	0.1	0.001
1	1	—	—	1028.42	34.4	0.1	0.003
1	1	—	—	1761.58	34.4	0.1	0.006

Table 1. The estimated values of $Ra_{\tau c}$ and k_c for the shallow chamber case are presented where -HP and -Present represent the values of Hillesdon & Pedley (1996) and the present work, respectively.

Among the ten sets of results, only six have been compared with the results of Hillesdon & Pedley (1996), which can be seen in table 1; the neutral stability curves $Ra_\tau(k)$ are plotted in figure 4 and figure 7 shows the variation of other parameters. The estimated results of $Ra_{\tau c}$ and the corresponding values of k_c vs $S_\tau H_\tau$ with the varying values of other parameters are visualized in figure 3. Some interesting points can be observed in these computed results of $Ra_{\tau c}$ and k_c. Firstly, we can see in figure 7(c) that the neutral curves for the different values of Le_τ (fixed $S_\tau H_\tau = 1$) diverge initially and then gradually converge as the wavenumber increases. Conversely, in the study by Hillesdon & Pedley (1996), neutral curves diverged for different values of δ_{HP} as the wavenumber increased (see figure 5 in Hillesdon & Pedley 1996). Secondly, the computed value of Ra_τ for a given k is larger for $Le_\tau = 10$ than for $Le_\tau = 1$, i.e. as Le_τ increases, the system stabilizes. The same trend can be seen in the work of Hillesdon & Pedley (1996). Interestingly, the computed values of $Ra_{\tau c}$ and k_c for the present study in case sets 2 and 8 are the same.
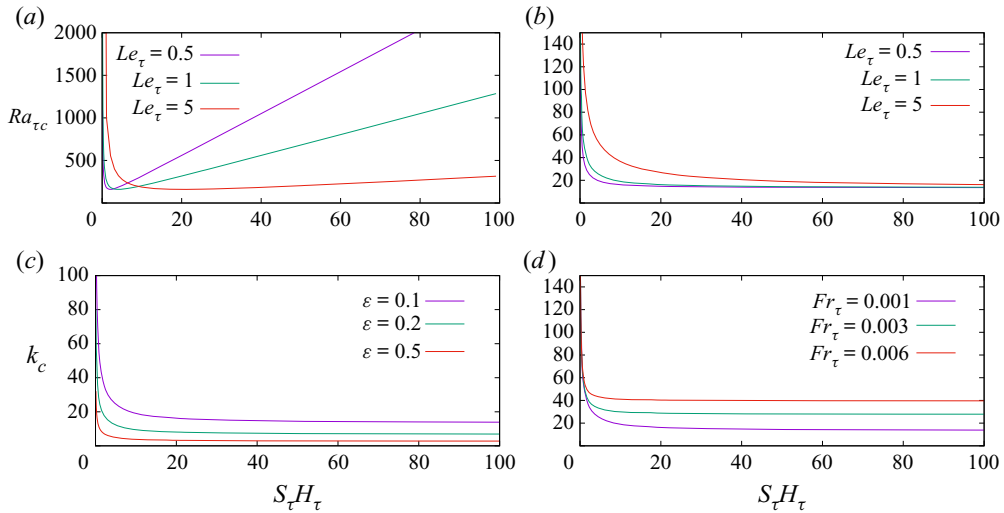
923 A14-14

Figure 3. (*a*) Critical values of Rayleigh number, $Ra_{\tau c}$, and (*b*) the corresponding values of the critical wavenumber are computed for varying Le_τ; (*c*) the variation of ε and (*d*) Froude numbers Fr_τ are shown for fixed values of $Le_\tau = 1$ and $Pr_\tau = 7700$. The minimum value in the curve is $S_\tau H_\tau / Le_\tau \approx 1.936$.
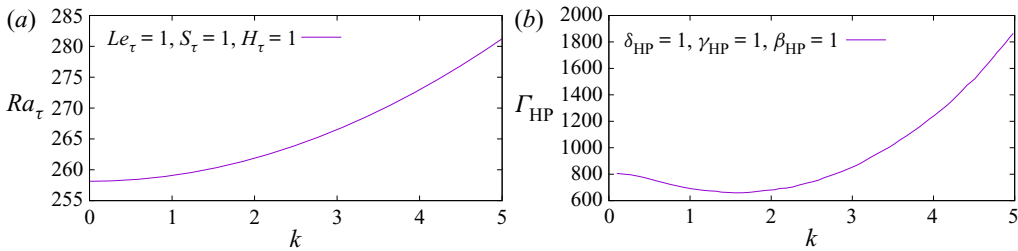

Figure 4. Comparison of the neutral stability curve of the present study (*a*) with the result of Hillesdon & Pedley (1996) (*b*) for shallow chamber.

The interpretation of these results is not straightforward. The increment in the value of Le_τ can be expressed either as an increase in D_O with fixed D_b or as a decrease in D_b with fixed D_O, and the decreasing value of Le_τ can be expressed *vice versa*. A difference can be seen between the present study and that of Hillesdon & Pedley (1996) for the case sets in table 1 and figure 4. In our study, the neutral stability curve for $Le_\tau = 1$, $S_\tau = 1$ and $H_\tau = 1$ slowly diverges initially and then gradually stabilizes as k increases, whereas for Hillesdon & Pedley (1996), it diverged for any given k.

It can be visualized from the table 1 that, with the increasing value of Le_τ, a plane free surface density gradient occurs for larger values of $S_\tau H_\tau$. However, the value of $Ra_{\tau c}$ first drops as $S_\tau H_\tau$ is increased and then rises again. Besides, k_c has a maximum value, although the minimum values of k_c and $Ra_{\tau c}$ are not obtained at the same value as $S_\tau H_\tau$. This behaviour is exhibited in figures 3(*a*) and 3(*b*), which show the critical Rayleigh number, $Ra_{\tau c}$, and the corresponding value of k_c being plotted against $S_\tau H_\tau$ for varying values of Le_τ. From the figure, we can see that, for each value of Le_τ, the minimum value of $Ra_{\tau c}$ is found when $S_\tau H_\tau / Le_\tau \approx 1.936$. From this detection, it is now clear that Ra_τ might not be suitable for measuring the ratio between the buoyancy force that leads to bioconvection and the viscous force that intercepts it.

S. Chakraborty and T.W.-H. Sheu

The frequency of oscillation vs $S_\tau H_\tau$ is plotted with the variation of Le_τ in figure 8(a). It can be observed from the figure that the growth rate is not affected by the variation of Le_τ. However, in the growth rate, the curve shift towards higher $S_\tau H_\tau$ becomes noticeable as the value of the Lewis number increases. This behavioural change is due to the increasing value of Le_τ. Hence, the cell diffusivity is extremely less than oxygen, i.e. a smaller cell concentration at the interface leads to greater discontinuity (the system becomes unstable). Besides, the presence of Fr_τ aids in increasing the cell concentration with increasing Le_τ.

The characteristics of the perturbed cell and oxygen concentrations and velocity profiles are illustrated in figures 10(a), 11(a) and 12(a), respectively, corresponding to the values of $Ra_{\tau c}$ and k_c for a shallow chamber with the variation of Le_τ. It is clear from figure 10(a) that, as the value of Le_τ increases, the concentration of cells decreases at the air–water interface, and their movement towards the free surface is steady. With decreasing Le_τ, the cells get denser, and the cells' movement towards the free surface is more rapid. The aggregation of cells is mostly found just below the layer of free surface. This result justifies that, when the oxygen diffusion is higher, then the cell diffusivity is small or constant, and so are the critical values of $Ra_{\tau c}$ and k_c, which start to fall with the increase of Le_τ. As Le_τ increases, the diffusivity of oxygen also increases, and this statement is supported by the oxygen concentration profiles presented in figure 11(a) for the variation of $Le_\tau = 0.5, 1, 5$. Figure 12(a) shows the characteristics of the perturbed fluid velocity profiles for a shallow chamber corresponding to the values of $Ra_{\tau c}$ and k_c. The intensity of the wave profile for $Le_\tau = 0.5$ is much higher than that for the case with the increasing value of Le_τ. Eventually, an increase in the diffusivity of oxygen makes the system unstable, and *vice versa*, as Le_τ decreases. The flow motion in the chemotaxis system is interrupted at the onset of convection, however, it stabilizes after reaching the free surface.

Thus far, the results have been compared when there is variation in Le_τ and the other physical parameters are fixed at $\varepsilon = 0.1$, $S_\tau H_\tau = 1$, $Pr_\tau = 7700$, $Fr_\tau = 0.001$ and $Ca_\tau = 0.01$. In the next stage, the impact of the Froude number is discussed by varying the Fr_τ values to $0.001, 0.003$ and 0.006 and fixing the other parameters at $Le_\tau = 1$, $\varepsilon = 0.1$, $S_\tau H_\tau = 1$, $Pr_\tau = 7700$ and $Ca_\tau = 0.01$. It is noteworthy that the results of figures 10, 11 and 12, are plotted from the eigenvalue problem.

4.2. *Vary Fr_τ; other parameters are fixed*

The values of $Ra_{\tau c}$ and k_c have been computed by varying the Froude number and presented in table 1. It can be observed from the parameter sets two, nine and ten that for $Fr_\tau = 0.001, 0.003$ and 0.006, the computed $Ra_{\tau c}$ values are 811.183, 1028.42 and 1761.58, respectively, whereas k_c gives the same value of 34.4 for different Fr_τ (here, $S_\tau H_\tau = 1$ and $Le_\tau = 1$). This situation is also illustrated in figure 3(d), where k_c vs $S_\tau H_\tau$ is plotted for the varying values of Fr_τ. Notably, under the variation of Fr_τ, k_c shows the same critical value at the minimum value of $S_\tau H_\tau$. This implies that the wavenumber is not influenced by the change in $S_\tau H_\tau$ though the initial jump found is due to the change in Fr_τ. As the value of the Froude number increases, the wavenumber reaches its maximum value in the uniform stage of the system. Otherwise, the wavenumber is constant throughout the system. In figure 7(d), neutral stability curves are shown under the variation of Fr_τ. Due to the presence of Fr_τ, the flow at the free surface accelerates under the action of gravity. As the value of Fr_τ increases, the flow accelerates even further for $Fr_\tau = 0.006$ compared with those at other values of Froude number. Therefore, initially, the system seems to be destabilized, however, it stabilizes as the wavenumber increases. However, if we look at the result of the oscillation of frequency curves in figure 8(c), it shows a minute deflation

923 A14-16

in the growth rate as Fr_τ increases. However, quite a big shift is noticed in the growth rate. The frequency of oscillations vs $S_\tau H_\tau$ is illustrated in figure 8(*c*) for the variation of Fr_τ. In other words, a decrease in the frequency of oscillations causes the system to become stabilized.

The real parts of the perturbed cell and oxygen concentrations and velocity profiles are plotted by varying $Fr_\tau = 0.001$, 0.003, and 0.006 in figures 10(*f*), 11(*f*) and 12(*e*), respectively, corresponding to the values of $Ra_{\tau c}$ and k_c. Both the cell and oxygen concentration profiles show a subtle effect on the upper surface rather than the bottom surface of the chemotaxis system. Although the differences are very small, the cell concentration profile decreases as Fr_τ increases with a steady motion and gradually reaches towards the free surface. The same situation is also seen for the perturbed oxygen concentration profiles. The significant effect of Fr_τ is visible at the perturbed fluid velocity profiles, where on increasing the value of Fr_τ, the velocity of the fluid becomes steady at the free surface. It stabilizes the motion of the fluid close to the free surface, where the concentrations of both cells and oxygen are balanced. Whereas the comparison between the profiles of N_r, C_r and W_r slightly differs for the higher value of Fr_τ.

4.3. *Vary Ca_τ; other parameters are fixed*

The frequency of oscillations vs $S_\tau H_\tau$ is illustrated in figure 8(*b*) for the variation of Ca_τ. The increasing value of Ca_τ shows an inflation in the growth rate along with a small shift, leading the system to be stable. The curves widen due to the increasing value of $S_\tau H_\tau$ as Ca_τ increases, and the peak value falls, giving stability to the system at the free surface in the shallow chamber case. The frequency of oscillation, ω, vs k is plotted in figure 9(*b*) for the variation of Ca_τ. The same scenario can be seen here for the frequency of oscillations where the curves get wider and the peaks rise with the increasing wavenumber, however, this occurs for the decreasing value of Ca_τ. A slight tilt in the front of the curves can be seen for the decreasing value of Ca_τ. This explains that the surface tension is tenacious enough to hold the exalted wave profile.

The real parts of the perturbed cell and oxygen concentrations, and velocity profiles are plotted by varying $Ca_\tau = 0.005$, 0.01, and 0.05 in figures 10(*e*), 11(*e*) and 12(*d*), respectively, which are corresponding to the values of $Ra_{\tau c}$ and k_c. A similar scenario can be seen in figures 10(*f*) and 11(*f*) for the variation of Fr_τ. Note that in figures 10(*e*) and 11(*e*) we mentioned the perturbed cell and oxygen concentrations for varying values of Ca_τ. Figure 12(*d*) shows the different characteristics of the perturbed fluid velocity profile W_r in a shallow chamber with the variation of Ca_τ. It is clear from the figure that the velocity profile W_r increases with an increasing value of Ca_τ. The comparison between the profiles of W_r (the perturbed fluid velocity), N_r (the perturbed cell concentration) and C_r (the perturbed oxygen concentration) detects a random movement of cells in the system as lack in oxygen makes the system unstable. The chemotaxis system stabilizes as the surface tension increases at the free surface. However, at the onset of convection, the system shows a destabilizing effect. The concentrations of cells and oxygen increase near the free surface, and almost all cells are accumulated near the stable free surface.

4.4. *Vary $S_\tau H_\tau$; other parameters are fixed*

In table 1, the estimated values of $Ra_{\tau c}$ and k_c for shallow chamber are given for the variation of $S_\tau H_\tau$ and Le_τ. These values of $Ra_{\tau c}$ and k_c are compared with those of Hillesdon & Pedley (1996) though the comparison by varying Le_τ has been discussed in the previous section. In linear stability analysis, we have fixed the value of Le_τ, and
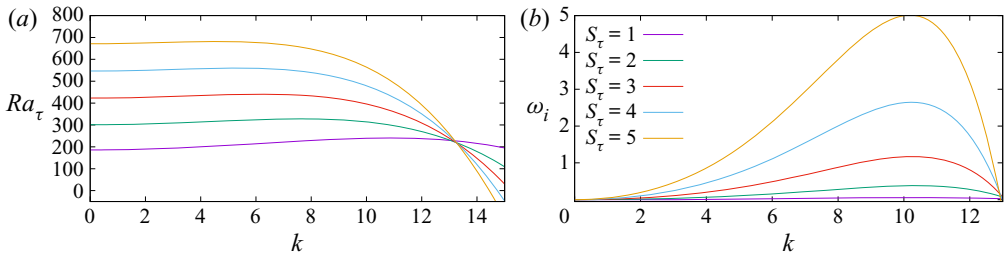
Figure 5. (*a*) The curves Ra_τ and (*b*) ω_i corresponding to varying values of S_τ at fixed values of $Le_\tau = 1$, $\varepsilon = 0.1$, $H_\tau = 10$, $Pr_\tau = 7700$, $Fr_\tau = 0.001$ and $Ca_\tau = 0.01$.
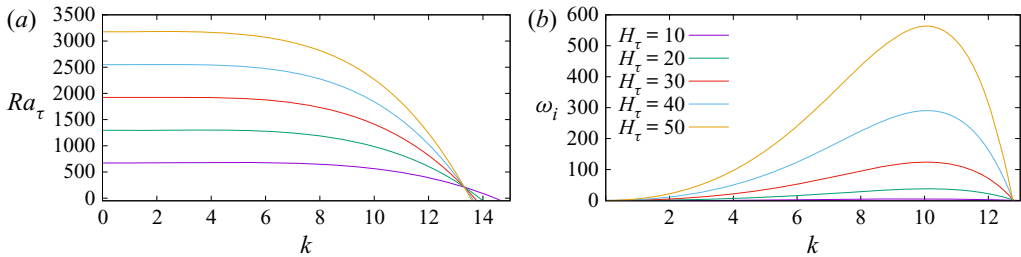

Figure 6. The curves Ra_τ and (*b*) ω_i corresponding to varying values of H_τ at fixed values of $Le_\tau = 1$, $\varepsilon = 0.1$, $S_\tau = 5$, $Pr_\tau = 7700$, $Fr_\tau = 0.001$ and $Ca_\tau = 0.01$.

independently varied the values of S_τ and H_τ. These variations can be seen in figures 5 and 6 are discussed in detail later in this section. In table 1, data sets 1–7, we have fixed the values of $Le_\tau = 1$ and $S_\tau = 1$, and varied H_τ from 0.05 to 100. It can be observed that, in the uniform stage of the system ($H_\tau = 0.05$), the critical Rayleigh number is estimated to take the highest value and similarly for the critical wavenumber. It can be seen that, as the value of H_τ increases, the value of the critical Rayleigh number drops. The minimum value of the critical Rayleigh number is found when $H_\tau = 10$. Then, the value of critical Rayleigh number starts to rise again as the value of H_τ starts increasing. When $k \to 0$, the analytical approximation is $Ra_\tau \to 1440Le_\tau/7S_\tau H_\tau = 4114.29$. The critical values of the Rayleigh number and wavenumber are $Ra_{\tau c} = 15234.24$ and $k_c = 154.4$. It can be anticipated that our numerically predicted first pattern would be experimentally seen when Ra_τ is slowly reduced to $Ra_{\tau c}$. In general, the most unstable disturbance occurred for $Ra_\tau > Ra_{\tau c}$, which has a different wavelength. The approximate value of a dimensionless wavelength $\lambda_c = 2\pi/k_c$ can be calculated from the value of the critical wavenumber k_c. It would be interesting to conduct an experiment using the present model to verify these estimated results and predictions.

In figures 5 and 6, the neutral stability and growth rate, respectively, are plotted with the variations of S_τ and H_τ separately. In figure 5, S_τ is varied from 1 to 5, and H_τ is varied from 10 to 50 in figure 6. Interestingly, all the neutral stability curves in figures 5(*a*) and 6(*a*) for the variation of S_τ and H_τ, respectively, intersect at a point when $Ra_\tau = 205.71$. Further, all the curves of the growth rate in figures 5(*b*) and 6(*b*) for the variation of S_τ and H_τ, respectively, have the cutoff wavenumber $k = 12.8$. In figures 5(*a*) and 6(*a*), all the neutral stability curves for different values S_τ and H_τ converge as the wavenumber increases. In fact, the value of Ra_τ, for a given k, is larger, for $S_\tau = 5$ and $H_\tau = 10$, than for the other lower varying values of S_τ and H_τ. It is implied that an increase in the
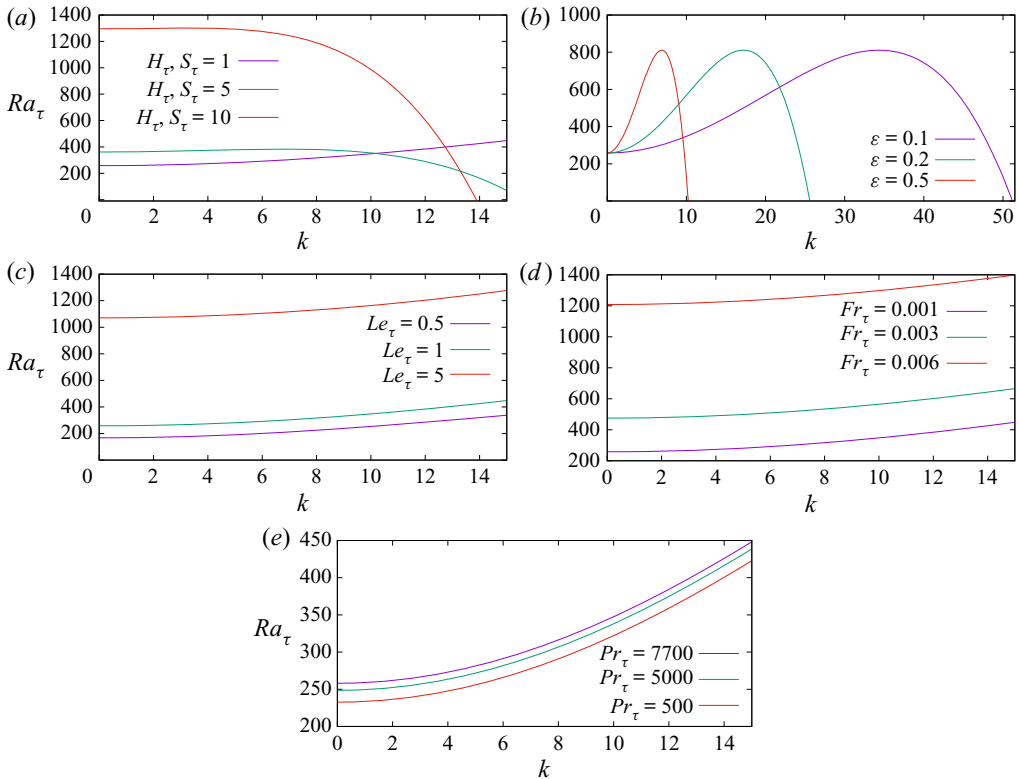
923 A14-18

Figure 7. Neutral stability curves presented with the variation of H_τ, S_τ in (*a*) (fixed $Le_\tau = 1$, $\varepsilon = 0.1$, $Pr_\tau = 7700$, $Ca_\tau = 0.01$, $Fr_\tau = 0.001$), ε in (*b*) (fixed $Le_\tau = 1$, S_τ, $H_\tau = 1$, $Pr_\tau = 7700$, $Ca_\tau = 0.01$, $Fr_\tau = 0.001$), Le_τ in (*c*) (fixed $\varepsilon = 0.1$, S_τ, $H_\tau = 1$, $Pr_\tau = 7700$, $Ca_\tau = 0.01$, $Fr_\tau = 0.001$), Fr_τ in (*d*) (fixed $Le_\tau = 1$, $\varepsilon = 0.1$, S_τ, $H_\tau = 1$, $Pr_\tau = 7700$, $Ca_\tau = 0.01$) and Pr_τ in (*e*) (fixed $Le_\tau = 1$, $\varepsilon = 0.1$, S_τ, $H_\tau = 1$, $Ca_\tau = 0.01$, $Fr_\tau = 0.001$).
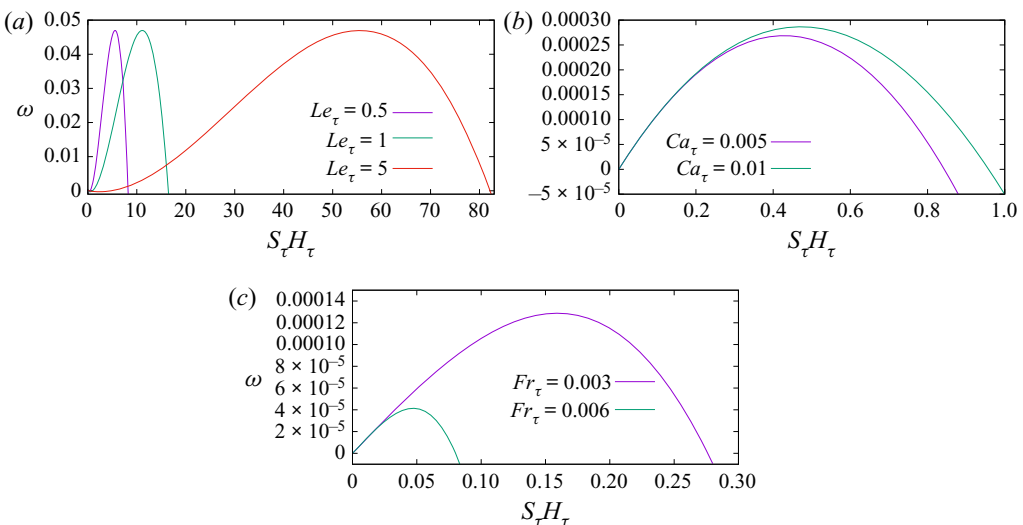

Figure 8. The curves of ω are presented at the critical Ra_τ with the variation of Le_τ in (*a*) (fixed $Ca_\tau = 0.01$, $Fr_\tau = 0.001$), Ca_τ in (fixed $Le_\tau = 1$, $Fr_\tau = 0.001$) (*b*) and Fr_τ in (fixed $Le_\tau = 1$, $Ca_\tau = 0.01$) (*c*).
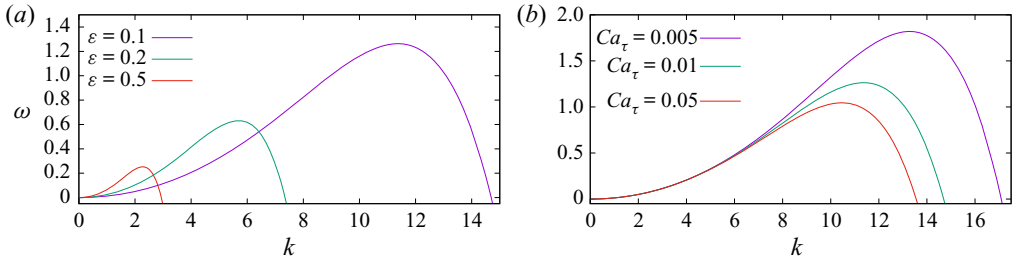
Figure 9. The curves of ω are presented at the critical Ra_τ with the variation of ε in (*a*) (fixed $Ca_\tau = 0.01$) and Ca_τ in (*b*) (fixed $\varepsilon = 0.1$). Other parameters are fixed at $Le_\tau = 1$, $S_\tau = 1$, $H_\tau = 1$, $Fr_\tau = 0.001$ and $Pr_\tau = 7700$.
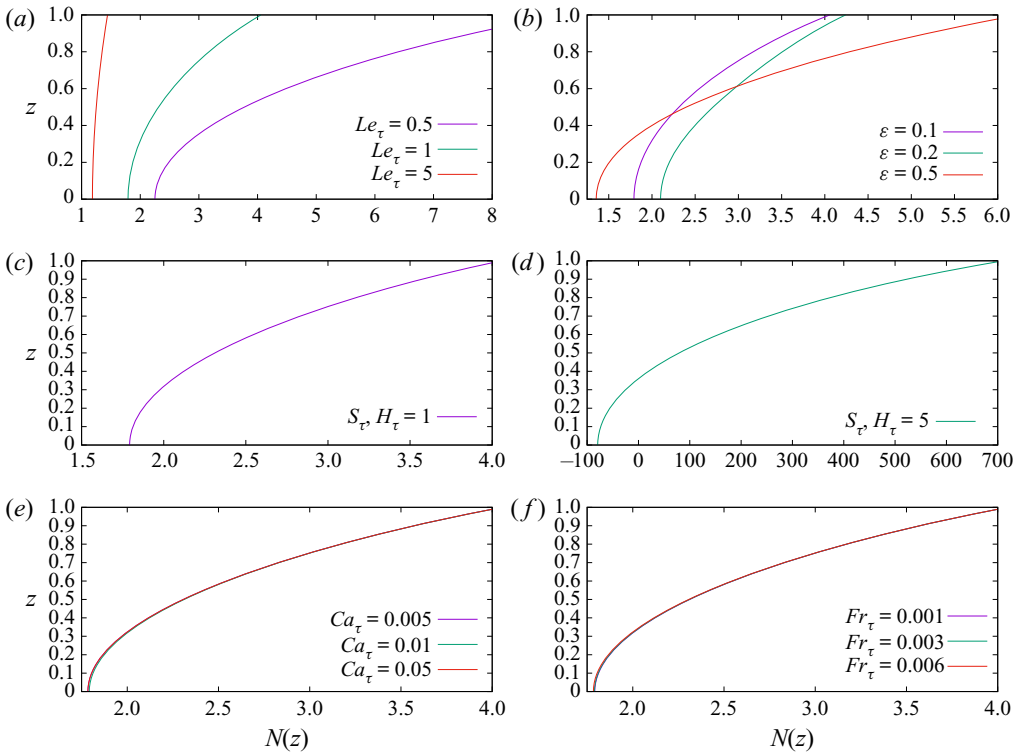

Figure 10. Different characteristics of the perturbed cell concentration profiles N_r are presented corresponding to the values of $Ra_{\tau c}$ and k_c for shallow chamber with the variation of Le_τ in (*a*) (fixed $\varepsilon = 0.1$, S_τ, $H_\tau = 1$, $Pr_\tau = 7700$, $Ca_\tau = 0.01$ and $Fr_\tau = 0.001$); ε in (*b*) (fixed $Le_\tau = 1$, S_τ, $H_\tau = 1$, $Pr_\tau = 7700$, $Ca_\tau = 0.01$ and $Fr_\tau = 0.001$); Ca_τ in (*e*) (fixed $\varepsilon = 0.1$, $Le_\tau = 1$, S_τ, $H_\tau = 1$, $Pr_\tau = 7700$ and $Fr_\tau = 0.001$); Fr_τ in (*f*) (fixed $\varepsilon = 0.1$, $Le_\tau = 1$, S_τ, $H_\tau = 1$, $Pr_\tau = 7700$ and $Ca_\tau = 0.01$). Panels (*c,d*) show the profiles for S_τ, $H_\tau = 1$ and S_τ, $H_\tau = 5$ and other parameters are fixed at $\varepsilon = 0.1$, $Le_\tau = 1$, $Pr_\tau = 7700$, $Ca_\tau = 0.01$ and $Fr_\tau = 0.001$.

values of S_τ and H_τ is evidently stabilizing. The qualitative behaviour in each case is the same, as the wavenumber k increases, the Rayleigh number Ra_τ decreases steadily to its minimum value. The variation in H_τ shows that the motion of fluid at the critical Rayleigh number consists of convective cells. Thus, the cells initiated in the upper unstable layer penetrate through the stable layer and reach towards the bottom layer. The convection starts in this situation, and soon, the whole chamber becomes involved in this motion. This initial motion, observed experimentally, has a wavenumber, and this wavenumber
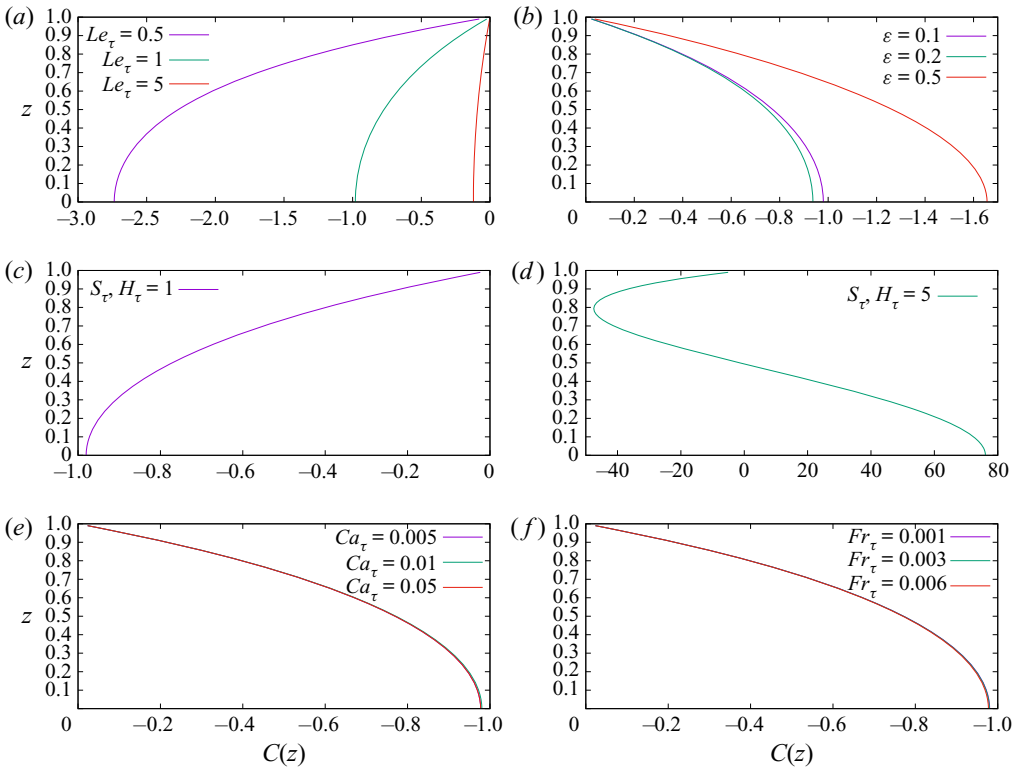
Figure 11. Different characteristics of the perturbed oxygen concentration profiles C_r are presented corresponding to the values of $Ra_{\tau c}$ and k_c for shallow chamber with the variation of Le_τ in (*a*) (fixed $\varepsilon = 0.1$, $S_\tau, H_\tau = 1$, $Pr_\tau = 7700$, $Ca_\tau = 0.01$ and $Fr_\tau = 0.001$); ε in (*b*) (fixed $Le_\tau = 1$, $S_\tau, H_\tau = 1$, $Pr_\tau = 7700$, $Ca_\tau = 0.01$ and $Fr_\tau = 0.001$); Ca_τ in (*e*) (fixed $\varepsilon = 0.1$, $Le_\tau = 1$, $S_\tau, H_\tau = 1$, $Pr_\tau = 7700$ and $Fr_\tau = 0.001$); Fr_τ in (*f*) (fixed $\varepsilon = 0.1$, $Le_\tau = 1$, $S_\tau, H_\tau = 1$, $Pr_\tau = 7700$ and $Ca_\tau = 0.01$). Panels (*c*,*d*) show the profiles for $S_\tau, H_\tau = 1$ and $S_\tau, H_\tau = 5$ and other parameters are fixed at $\varepsilon = 0.1$, $Le_\tau = 1$, $Pr_\tau = 7700$, $Ca_\tau = 0.01$ and $Fr_\tau = 0.001$.

is presumed to be equal to the most unstable wavenumber corresponding to the value of Ra_τ. Similarly, the growth rates in figures 5(*b*) and 6(*b*) show higher inflation for large values of S_τ and H_τ, i.e. increase in S_τ and H_τ is apparently stabilizing. The growth rate corresponding to a particular wavenumber is greatest in $S_\tau = 5$ and $H_\tau = 50$, for $k > 4$.

In figures 10(*d*) and 10(*c*), 11(*d*) and 11(*c*) and 12(*c*), the characteristics of the perturbed cell and oxygen concentrations, and the fluid velocity profiles, respectively, are presented with respect to the length of the shallow chamber corresponding to the values of $Ra_{\tau c}$ and k_c. In figures 10(*d*) and 10(*c*), H_τ is varied from 1 to 5, respectively, whereas S_τ is fixed at 1. The concentration of cells for $H_\tau = 1$ is less at the bottom of the chamber and increases near the free surface (see figure 10*d*). Moreover, in figure 10(*c*), the concentration of cells for $H_\tau = 5$ is even lower than that for $H_\tau = 1$, and, similarly, it increases near the free surface. In figures 10(*d*) and 10(*c*), the concentration of oxygen gradually increases for $H_\tau = 1$ as moving towards the free surface. Moreover, as expected, the most apparent difference is seen in the C_r distribution profile for $H_\tau = 5$. Although, both cell and oxygen zero-flux conditions are satisfied at $z = 0$. The distribution of C is mostly interrupted within the system due to the excessive consumption of the oxygen. The fluid velocity profile W_r increases with the increasing value of H_τ (see in figure 12*c*). The difference in the velocity profiles becomes more noticeable as the value of H_τ increases.
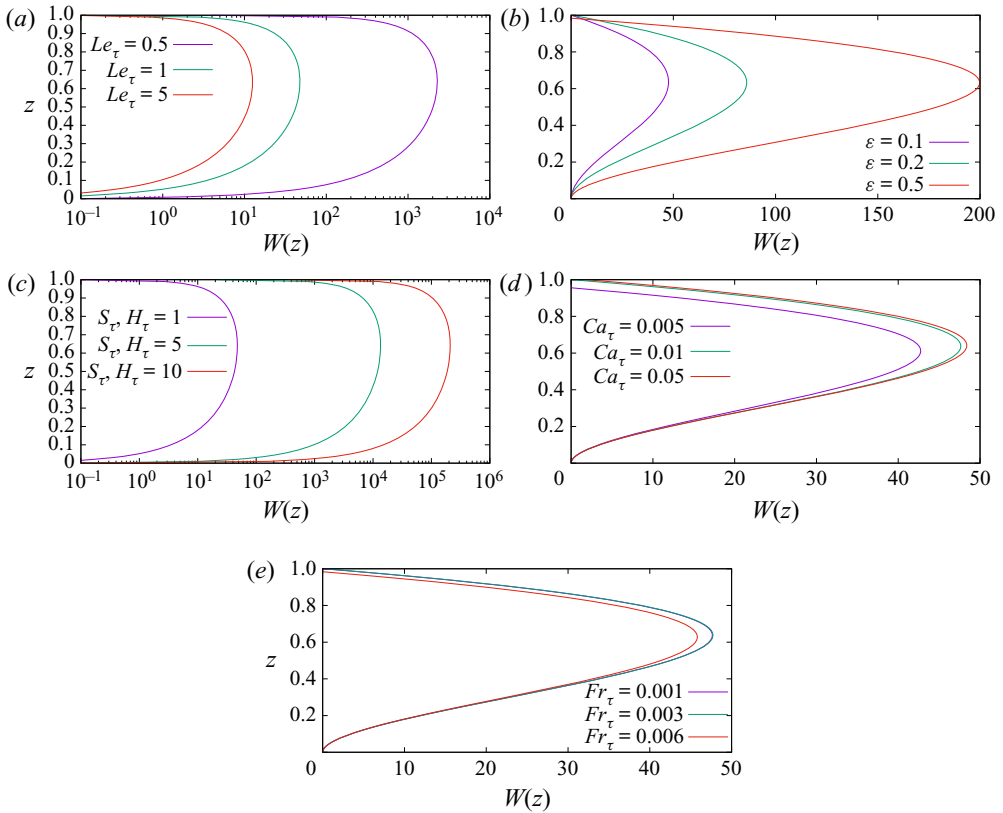
Figure 12. Different characteristics of the perturbed fluid velocity profiles W_r are presented corresponding to the values of $Ra_{\tau c}$ and k_c for shallow chamber with the variation of Le_τ in (*a*) (fixed $\varepsilon = 0.1$, S_τ, $H_\tau = 1$, $Pr_\tau = 7700$, $Ca_\tau = 0.01$ and $Fr_\tau = 0.001$); ε in (*b*) (fixed $Le_\tau = 1$, S_τ, $H_\tau = 1$, $Pr_\tau = 7700$, $Ca_\tau = 0.01$ and $Fr_\tau = 0.001$); S_τ, H_τ in (*c*) (fixed $\varepsilon = 0.1$, $Le_\tau = 1$, $Pr_\tau = 7700$, $Ca_\tau = 0.01$ and $Fr_\tau = 0.001$); Ca_τ in (*d*) (fixed $\varepsilon = 0.1$, $Le_\tau = 1$, S_τ, $H_\tau = 1$, $Pr_\tau = 7700$ and $Fr_\tau = 0.001$); Fr_τ in (*e*) (fixed $\varepsilon = 0.1$, $Le_\tau = 1$, S_τ, $H_\tau = 1$, $Pr_\tau = 7700$ and $Ca_\tau = 0.01$).

4.5. *Variation of ε and Pr_τ*

The length of the shallow chamber has also been varied to investigate the nature of the stability and the impact of ε on the present system. The variation of ε presented in table 1 shows that the estimated values of $Ra_{\tau c}$ remained unchanged for different ε although the estimated values of k_c increased with decreasing ε. It can be said that the number of waves increases as the length of the chamber increases. These results are illustrated in figure 3(*c*) where one can clearly visualize that the critical wavenumber increases with the decreasing value of ε and is not influenced by the change in $S_\tau H_\tau$. This statement can also be verified through figure 7(*b*), in which the neutral stability curves show a stabilizing effect in the increasing cutoff wavenumber when the length of the chamber increases although Ra_τ is not influenced by the change. The impact of the chamber length can also be seen in the frequency of oscillations, where the growth rate is illustrated against the wavenumber in figure 9(*a*).

In figures 10(*b*), 11(*b*) and 12(*b*), the characteristics of the perturbed cell and oxygen concentrations, and fluid velocity profiles, respectively, are presented with the variation in the length of the shallow chamber corresponding to the values of $Ra_{\tau c}$ and k_c. It can
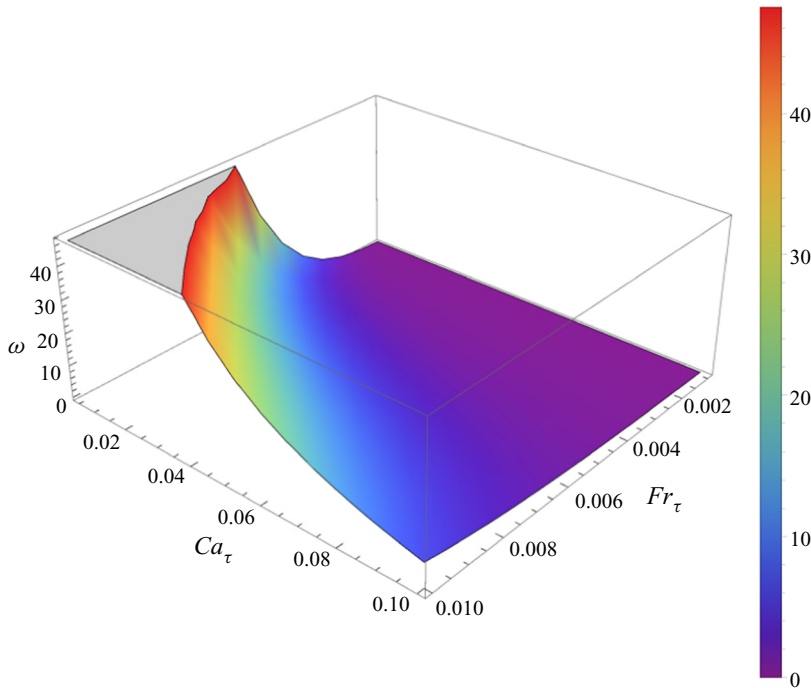
Figure 13. Frequency of oscillation, ω, is plotted for the variations of Ca_τ and Fr_τ corresponding to the values of $Ra_{\tau c}$ and k_c for shallow chamber, and other parameters are fixed at $\varepsilon = 0.1$, $Le_\tau = 1$, $S_\tau = 1$, $H_\tau = 10$ and $Pr_\tau = 7700$.

be observed in figure 10(b) that the cell concentrations at the free surface for a small chamber are lower than in the long chamber in comparison with those at the bottom of the shallow chamber. Therefore, it can be stated that the cell concentration will increase with an increasing length of the chamber. However, the oxygen concentration profiles in figure 11(b) show that the oxygen concentration level will be identical at the free surface for differently sized chambers although at the bottom of the chamber, the oxygen concentration level will increase/decrease as the length of the chamber decreases/increases. Figure 12(b) shows that the variation in the length of the chamber has a significant impact on the velocity of the wave profiles. As the length of the chamber increases, we can observe steady velocity profiles, whereas the velocity of the wave profile increases as the length of the chamber decreases.

We have varied Pr_τ from $500 \sim 7700$ to investigate the impact of the Prandtl number on the chemotaxis system, and this is shown in figure 7(e). It can be observed from the figure that the trend of the curves is similar for the variation of Pr_τ. As Pr_τ increases, the value of Ra_τ increases along with the value of wavenumber. Here, Pr_τ is defined as the ratio of the fluid diffusivity to cell diffusivity, and the values are varied for $500 \leqslant Pr_\tau \leqslant 7700$, i.e. the viscosity of the fluid is higher than the cell diffusivity, and this brings instability to the chemotaxis system. Since all the curves show a similar nature in the figure, so the highest value of $Pr_\tau (=7700)$ is considered for the parametric study.

Since Fr_τ and Ca_τ are two important physical parameters in this system, we have varied both the parameters together as well as the other parameters such as Le_τ and ε to study their influence on the stability of the chemotaxis system. The frequency of oscillations, ω, vs Fr_τ and Ca_τ is plotted in figure 13. The figure shows that the peak of the frequency
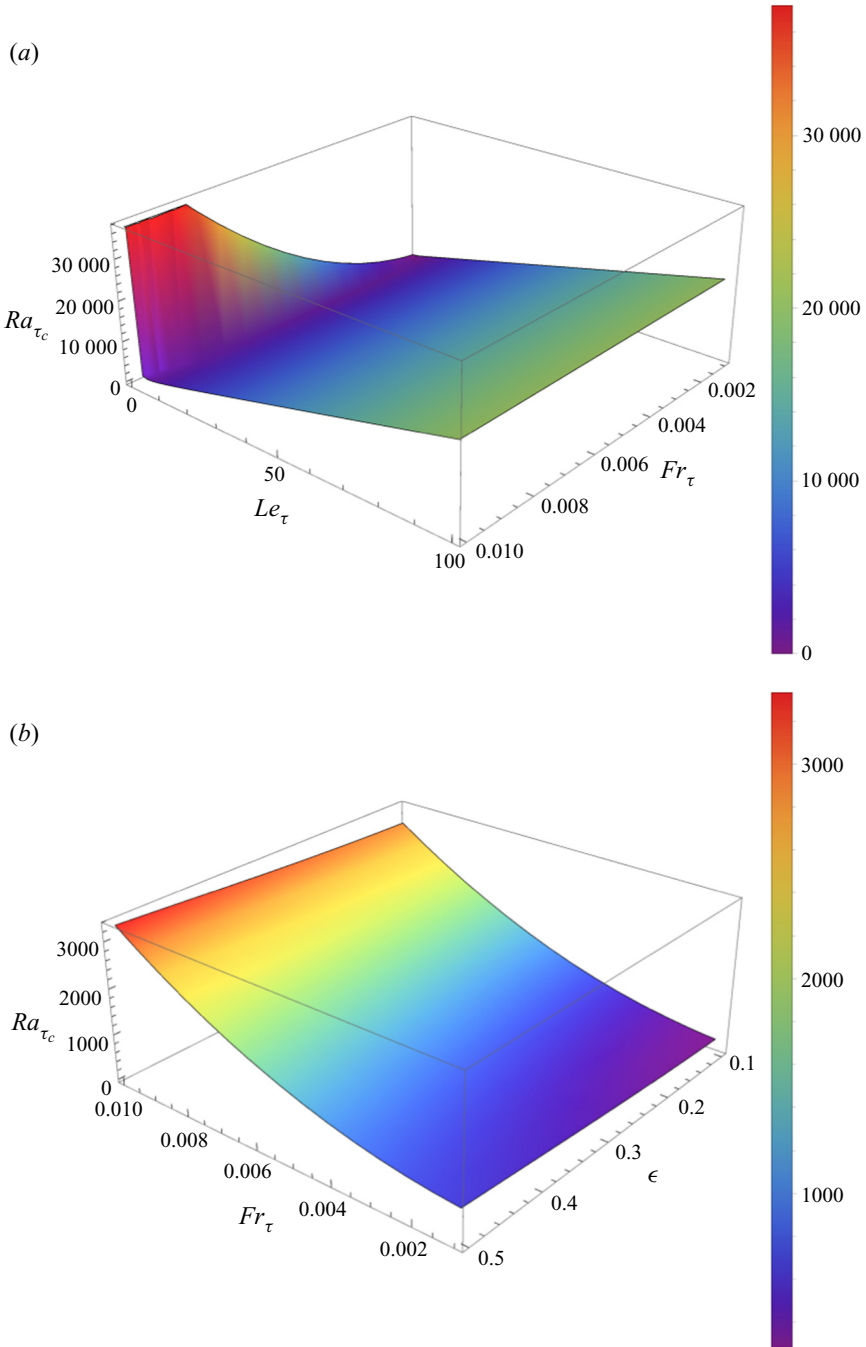
923 A14-23

(*a*)

(*b*)

Figure 14. Critical Rayleigh number, $Ra_{\tau c}$, is plotted for the variations of Le_τ and Fr_τ ($\varepsilon = 0.1$ fixed) in (*a*), and for the variations of ε and Fr_τ ($Le_\tau = 1$) in (*b*). Other parameters are fixed at $S_\tau = 1, H_\tau = 1, Ca_\tau = 0.01$ and $Pr_\tau = 7700$.

of the oscillation curve increases with a decreasing value of Ca_τ, and the increase in the peak of the curve is also influenced by an increasing value of Fr_τ. The curve exponentially increases with the increasing value of Fr_τ. Based on the results in the figure, we can say that the surface tension force is strong enough to hold the peak of the wave, although increasing the value of Fr_τ enables the curve to take its peak value. Then, at a much lower value of Ca_τ and higher value of Fr_τ, the frequency of the oscillation curve converges indicating the stabilization of the chemotaxis system.

The critical Rayleigh number, $Ra_{\tau c}$, vs Le_τ and Fr_τ is plotted in figure 14(a), and in figure 14(b), plotted against ε and Fr_τ. It can be seen in figure 14(a) that the value of Ra_τ drops initially when the value of Le_τ is smaller, however, then it diverges as the value of Le_τ increases. Here, it is worth mentioning that $Ra_{\tau c}$ also depends on the parameters S_τ and H_τ. The values of S_τ and H_τ are fixed to one here. Moreover, we have already seen in figure 3(a) how the neutral stability curve initially diverges at a small value of $S_\tau H_\tau$ for the lower value of Le_τ although, with an increasing value of Fr_τ, the neutral stability curve exponentially increases, showing the destabilizing nature of the system. However, after reaching a certain value of Fr_τ, the neutral stability curve converges. This effectively explains that the presence of Fr_τ in the system accelerates the fluid motions, however, an increase/decrease in the diffusivities of oxygen and cells would not affect the fluid motion. The fluid motion is affected due to the change in Fr_τ and $S_\tau H_\tau$. For the variations in Fr_τ, the impact on the neutral stability curve can easily be seen in figure 14(b). Although change in the value of ε does not have any impact on $Ra_{\tau c}$, the fluid motion is influenced due to the change in the length of the shallow chamber. It has been seen that the fluid accelerates even faster as the length of the chamber decreases. The number of waves that will occur in the system depends on the value of ε, as ε increases/decreases, the number of waves decreases/increases.

5. Conclusions

A three-dimensional model of the chemotaxis–convection–diffusion coupling system with the effect of surface tension at the air–water interface is considered. The impact of the surface tension on bioconvection, and *vice versa*, is the novelty of the present work, and it has been studied in detail. Both the surface tension phenomenon and cell dynamics at the free surface have been considered by incorporating them into the present model.

A parametric study of the chemotaxis–convection–diffusion system with deformed free surface with the effect of surface tension is performed. The parameters Le_τ, $S_\tau H_\tau$, Pr_τ, ε, Fr_τ and Ca_τ are varied and compared with the results of Hillesdon & Pedley (1996) for the flat free surface. The results of neutral stability curves showed that our system slowly starts to diverge initially, however, it stabilizes the system as k increases where the neutral stability curves always diverge for variation of parameter values in Hillesdon & Pedley (1996) study. As the value of Fr_τ increases, the value of the critical Ra_τ number increases, and this accelerates the free surface instability, although the wavenumber is not affected due to the increment in Fr_τ. The value of Ra_τ is independent of Ca_τ, but the flow velocity profile is influenced by the variation of Ca_τ. On variations in Ca_τ and Fr_τ, the cell and oxygen concentration profiles, respectively, show very small changes. Moreover, initially, the cells move towards the free surface (higher concentration of oxygen) and such a movement is not affected in the presence of the Froude number and surface tension. Later on, the cells are influenced and accelerated, and they accumulate near the trough of the waves. The variation in ε shows that the wavenumber increases as the length of the chamber increases. The frequency of oscillations is also increased with the increasing

wavenumber as the length of the chamber increases. Increase in the value of Le_τ and independent variation of S_τ and H_τ evidently stabilizes the system.

Linear stability analysis provides useful results on qualitative perspective of the unstable behaviour of the cell distribution at the onset of bioconvection, but it cannot explicate the initial stage of the formation of bioconvection patterns. Therefore, we expanded our study to perform weakly nonlinear stability analysis. It is observed in the linear stability analysis that the angular frequency or growth rate shows stability in the nature of the chemotaxis system at higher order. For this reason, we restrict the expansion of physical variables for the weakly nonlinear stability analysis up to the third order only. The parameter Ra_τ is the nonlinear controlled parameter of the chemotaxis system. In the near future, we will provide a complete weakly nonlinear stability analysis that will aid us in determining the nonlinear dynamics of the chemotaxis phenomenon and the stability of the formation of patterns at the onset of bioconvection on the free surface under the influence of surface tension. Also, we will provide the bifurcation theory results and compare them with the numerical simulation results. Due to the lack of experimental evidence for the present bioconvection model, it would be difficult to compare the results for validation.

Author ORCIDs.
S. Chakraborty https://orcid.org/0000-0002-6115-7859.

Appendix A. Solutions of N, $\bar{C}$ and W at $O(S_\tau H_\tau/Le_\tau)$, $O(S_\tau H_\tau/Le_\tau)^2$ and $O(S_\tau H_\tau/Le_\tau)^3$

The solutions of N_1, $\bar{C}_1$ and W_1 at the first order $O(S_\tau H_\tau/Le_\tau)$ are

$$
\begin{aligned}
W_1(z) = &-\frac{\tilde{k}^2 z^2 \varepsilon Ra_{\tau-1}}{6s!2Pr_\tau}[-240\tilde{k}^2\varepsilon^2 Fr_\tau{}^2 Pr_\tau{}^2 + 2(z-1)Pr_\tau(2z^3(\tilde{k}^2\varepsilon^2+1) + z^2(2-10\tilde{k}^2\varepsilon^2) \\
&+ z(5\tilde{k}^2\varepsilon^2 + 32) + 35\tilde{k}^2\varepsilon^2 - 128) + \tilde{k}^2\varepsilon^2(-2z^4 + 12z^3 - 15z^2 - 20z + 25)] \\
&+ \frac{\tilde{k}^4 z^2 \varepsilon^3 (Ra_{\tau-1})^2}{11!4Pr_\tau}[-5!1078 Fr_\tau{}^2 Pr_\tau{}^2 + 2(10z^9 - 88z^8 + 165z^7 - 539z^4 + 2475z^2 \\
&- 4070z + 2047)Pr_\tau - 539(2z^4 - 12z^3 + 15z^2 + 20z - 25)] \\
&- \frac{1}{24}\tilde{k}^2(z-3)(z-1)z^2\varepsilon Ra_{\tau 0},
\end{aligned}
\tag{A1a}
$$

$$
\begin{aligned}
\bar{C}_1(z) = &\frac{\tilde{k}^2\varepsilon^2 Ra_{\tau-1}}{9!2}[-10z^9 + 72z^8 - 108z^7 + 147z^4 - 270z^2 + 169] \\
&+ \frac{1}{24}(z^2-1)[z^2(\tilde{k}^2\varepsilon^2+2) - 5\tilde{k}^2\varepsilon^2 + 14],
\end{aligned}
\tag{A1b}
$$

$$
N_1(z) = 1 + z^2 - \frac{\tilde{k}^2\varepsilon^2 Ra_{\tau-1}}{7!4}(20z^7 - 112z^6 + 126z^5 - 49z^2 + 15).
\tag{A1c}
$$

At the second order, the governing equations are

$$\frac{d^4 W_2}{dz^4} = -\tilde{k}^2 \varepsilon (N_0 Ra_{\tau 1} - N_1 Ra_{\tau 0} - N_2 Ra_{\tau -1}) - \frac{\tilde{k}^2 \varepsilon^3}{Pr_\tau}(\tilde{k}^2 \varepsilon Pr_\tau + \omega_1) W_0$$

$$+ \frac{\varepsilon}{Pr_\tau}(2\tilde{k}^2 \varepsilon Pr_\tau + \omega_1)\frac{d^2 W_1}{dz^2} + \frac{\varepsilon \omega_2}{Pr_\tau}\frac{d^2 W_0}{dz^2}, \tag{A2}$$

$$\frac{d^2 N_2}{dz^2} = z\frac{d\bar{C}_0}{dz} + (\tilde{k}^2 \varepsilon^2 + \omega_1 \varepsilon + 2)N_1 + \frac{1}{3}(3z^2 + 3\omega_2 \varepsilon - 1)N_0 + \frac{1}{6}z(z^2 - 1)\frac{dN_0}{dz}$$

$$+ z\frac{dN_1}{dz} - \frac{1}{3}z(1 - 2z^2)\varepsilon W_0 + z\varepsilon W_1, \tag{A3}$$

$$\frac{d^2 \bar{C}_2}{dz^2} = \tilde{k}^2 \varepsilon^2 C_1 + N_2, \tag{A4}$$

with the boundary conditions

$$\left.\begin{array}{l}
\dfrac{d^3 W_2(1)}{dz^3} + \tilde{k}^2 \varepsilon^2 \dfrac{dW_1(1)}{dz} = 0, \\[2mm]
W_2(1) + \tilde{k}^2 \varepsilon^2 \dfrac{Fr_\tau^2 Pr_\tau}{Ca_\tau} W_1(1) + 2\varepsilon Fr_\tau^2 Pr_\tau \left(\omega_1 \dfrac{dW_1(1)}{dz} + \omega_2 \dfrac{dW_0(1)}{dz}\right) = 0, \\[2mm]
\bar{C}_2(1) = 0, \quad \dfrac{dN_2(1)}{dz} + \dfrac{\omega_2}{\omega_1}\dfrac{dN_1(1)}{dz} + + \dfrac{\omega_3}{\omega_1}\dfrac{dN_0(1)}{dz} - N_1(1) - \dfrac{\omega_2}{\omega_1}N_0(1) \\[2mm]
-\dfrac{d\bar{C}_1(1)}{dz} - \left(\dfrac{\omega_2}{\omega_1} + \dfrac{1}{3}\right)\dfrac{d\bar{C}_0(1)}{dz} - \dfrac{1}{2\omega_1}W_0(1) = 0, \\[2mm]
\dfrac{dW_2(0)}{dz} = 0, \quad W_2(0) = 0, \quad \dfrac{dN_2(0)}{dz} = 0, \quad \dfrac{d\bar{C}_2(0)}{dz} = 0.
\end{array}\right\} \tag{A5}$$

At the third order, the governing equations are

$$\frac{d^4 W_3}{dz^4} = -\tilde{k}^2 \varepsilon \left(N_0 Ra_{\tau 2} + N_1 Ra_{\tau 1} + N_2 Ra_{\tau 0} + N_3 Ra_{\tau -1}\right) + \frac{\varepsilon(2\tilde{k}^2 \varepsilon Pr_\tau + \omega_1)}{Pr_\tau}\frac{d^2 W_2}{dz^2}$$

$$+ \frac{\omega_2 \varepsilon}{Pr_\tau}\frac{d^2 W_1}{dz^2} + \frac{\omega_3 \varepsilon}{Pr_\tau}\frac{d^2 W_0}{dz^2} - \frac{\tilde{k}^2 \omega_2 \varepsilon^3}{Pr_\tau}W_0 - \frac{\tilde{k}^2 \varepsilon^3(\tilde{k}^2 \varepsilon Pr_\tau + \omega_1)}{Pr_\tau}W_1, \tag{A6}$$

$$\frac{d^2 N_3}{dz^2} = -\frac{1}{3}z(1 - 2z^2)\frac{d\bar{C}_0}{dz} + z\frac{d\bar{C}_1}{dz} + N_2(\tilde{k}^2 \varepsilon^2 + \omega_1 \varepsilon + 2) + \frac{1}{3}N_1(3z^2 + 3\omega_2 \varepsilon - 1)$$

$$+ \frac{1}{6}z(z^2 - 1)\frac{dN_1}{dz} + \frac{1}{18}N_0(3z^4 - 3z^2 + 18\omega_3 \varepsilon + 1) + z\frac{dN_2}{dz} - \frac{1}{3}z(1 - 2z^2)\varepsilon W_1$$

$$+ z\varepsilon W_2, \tag{A7}$$

$$\frac{d^2 \bar{C}_3}{dz^2} = \tilde{k}^2 \varepsilon^2 C_2 + N_3, \tag{A8}$$

with the boundary conditions

$$
\left.
\begin{aligned}
&\frac{\mathrm{d}^3 W_3(1)}{\mathrm{d}z^3} + \tilde{k}^2 \varepsilon^2 \frac{\mathrm{d}W_2(1)}{\mathrm{d}z} = 0, \\
&W_3(1) + \tilde{k}^2 \varepsilon^2 \frac{Fr_\tau{}^2 Pr_\tau}{Ca_\tau} W_2(1) + 2\varepsilon Fr_\tau{}^2 Pr_\tau \left(\omega_1 \frac{\mathrm{d}W_2(1)}{\mathrm{d}z} + \omega_2 \frac{\mathrm{d}W_1(1)}{\mathrm{d}z} + \omega_3 \frac{\mathrm{d}W_0(1)}{\mathrm{d}z} \right) = 0, \\
&\bar{C}_2(1) = 0, \qquad \frac{\mathrm{d}N_3(1)}{\mathrm{d}z} - \frac{(\omega_1 + 3\omega_2)}{3\omega_1} \frac{\mathrm{d}\bar{C}_1(1)}{\mathrm{d}z} - \frac{(6\omega_2 + 18\omega_3 + 1)}{18\omega_1} \frac{\mathrm{d}\bar{C}_0(1)}{\mathrm{d}z} - \frac{\mathrm{d}\bar{C}_2(1)}{\mathrm{d}z} \\
&+ \frac{\omega_3}{\omega_1} \frac{\mathrm{d}N_1(1)}{\mathrm{d}z} + \frac{\omega_2}{\omega_1} \frac{\mathrm{d}N_2(1)}{\mathrm{d}z} - \frac{\omega_3}{\omega_1} N_0(1) - \frac{\omega_2}{\omega_1} N_1(1) - N_2(1) - \frac{W_1(1)}{2\omega_1} - \frac{W_0(1)}{54\omega_1} = 0, \\
&\frac{\mathrm{d}W_3(0)}{\mathrm{d}z} = 0, \quad W_3(0) = 0, \quad \frac{\mathrm{d}N_3(0)}{\mathrm{d}z} = 0, \quad \frac{\mathrm{d}\bar{C}_3(0)}{\mathrm{d}z} = 0.
\end{aligned}
\right\}
$$

$$(A9)$$

REFERENCES

AVRAMENKO, A.A. & KUZNETSOV, A.V. 2010 Bio-thermal convection caused by combined effects of swimming of oxytactic bacteria and inclined temperature gradient in a shallow fluid layer. *Intl J. Numer. Meth. Heat Fluid Flow* **20** (2), 157–173.

BEES, M.A. 1998 Non-linear pattern generation by swimming micro-organisms. PhD thesis, University of Leeds.

BESTEHORN, M. 2009 Fluid dynamics, pattern formation. In *Encyclopedia of Complexity and System Science* (ed. R.A. Meyers). Springer.

BRENNER, M.P., LEVITOV, L.S. & BUDRENE, E.O. 1998 Physical mechanisms for chemotactic pattern formation by bacteria. *Biophys. J.* **74** (4), 1677–1693.

CHAKRABORTY, S., IVANCIC, F., SOLOVCHUK, M. & SHEU, T.W.H. 2018 Stability and dynamics of a chemotaxis system with deformed free-surface in a shallow chamber. *Phys. Fluids* **30** (7), 071904.

CHERTOCK, A., FELLNER, K., KURGANOV, A., LORZ, A. & MARKOWICH, P.A. 2012 Sinking, merging and stationary plumes in a coupled chemotaxis-fluid model: a high-resolution numerical approach. *J. Fluid Mech.* **694**, 155–190.

COMER, J. 2007 Pattern formation by swimming microorganisms. https://guava.physics.uiuc.edu/~nigel/courses/569/Essays_Fall2007/files/comer.pdf.

DELEUZE, Y., CHIANG, C.Y., THIRIET, M. & SHEU, T.W.H. 2016 Numerical study of plume patterns in a chemotaxis-diffusion-convection coupling system. *Comput. Fluids* **126**, 58–70.

DOEDEL, E.J. 2008 Auto07p continuation and bifurcation software for ordinary differential equations. *Tech. Rep.* Montreal Concordia University.

DUAN, R., LORZ, A. & MARKOWICH, P. 2010 Global solutions to the coupled chemotaxis-fluid equations. *Commun. Part. Diff. Equ.* **35**, 1635–1673.

HILL, N.A. & PEDLEY, T.J. 2005 Bioconvection. *Fluid Dyn. Res.* **37**, 1–20.

HILL, N.A., PEDLEY, T.J. & KESSLER, J.O. 1989 Growth of bioconvection patterns in a suspension of gyrotactic micro-organisms in a layer of finite depth. *J. Fluid Mech.* **208**, 509–543.

HILLESDON, A.J. 1994 Pattern formation in a suspension of swimming bacteria. PhD thesis, University of Leeds.

HILLESDON, A.J. & PEDLEY, T.J. 1996 Bioconvection in suspensions of oxytactic bacteria: linear theory. *J. Fluid Mech.* **324** (10), 223–259.

HILLESDON, A.J., PEDLEY, T.J. & KESSLER, J.O. 1995 The development of concentration gradients in a suspension of chemotactic bacteria. *Bull. Math. Biol.* **57** (2), 299–344.

IVANČIĆ, F., SHEU, T.W.H. & SOLOVCHUK, M. 2019 The free surface effect on a chemotaxis-diffusion-convection coupling system. *Comput. Meth. Appl. Mech. Engng* **356**, 387–406.

KELLER, E.F. & SEGEL, L.A. 1971 Model for chemotaxis. *J. Theor. Biol.* **30** (2), 225–234.

KESSLER, J.O., HOELZER, M.A., PEDLEY, T.J. & HILL, N.A. 1994 Functional patterns of swimming bacteria. In *Mechanics and Physiology of Animal Swimming* (ed. L. Maddock, Q. Bone & J.M.V. Rayner), pp. 3–12. Cambridge University Press.

Ko, W.H. & Chase, L.L. 1973 Aggregation of zoospores of *Phytophthora palmivora*. *J. Gen. Microbiol.* **78**, 79–82.

Kowalczyk, R., Gamba, A. & Preziosi, L. 2004 On the stability of homogeneous solutions to some aggregation models. *J. Discrete Continuous Dyn. Syst.* **4** (1), 203–220.

Kuznetsov, A.V. 2005 Investigation of the onset of thermo-bioconvection in a suspension of oxytactic microorganisms in a shallow fluid layer heated from below. *Theor. Comput. Fluid Dyn.* **19** (4), 287–299.

Lee, H.G. & Kim, J. 2015 Numerical investigation of falling bacterial plumes caused by bioconvection in a three-dimensional chamber. *Eur. J. Mech. (B/Fluids)* **52**, 120–130.

Liu, J.G. & Lorz, A. 2011 A coupled chemotaxis-fluid model: global existence. *Ann. Inst. Henri Poincaré* **28**, 643–652.

Ma, M., Gao, M., Tong, C. & Han, Y. 2016 Chemotaxis-driven pattern formation for a reaction-diffusion-chemotaxis model with volume-filling effect. *Comput. Math. Appl.* **72**, 1320–1340.

Metcalfe, A.M. & Pedley, T.J. 1998 Bacterial bioconvection: weakly nonlinear theory for pattern selection. *J. Fluid Mech.* **370**, 249–270.

Metcalfe, A.M. & Pedley, T.J. 2001 Falling plumes in bacterial bioconvection. *J. Fluid Mech.* **445**, 121–149.

Patlak, C.S. 1953 Random walk with persistence and external bias. *Bull. Math. Biophys.* **15**, 311–338.

Pedley, T.J., Hill, N.A. & Kessler, J.O. 1988 The growth of bioconvection patterns in a uniform suspension of gyrotactic micro-organisms. *J. Fluid Mech.* **195**, 223–237.

Pedley, T.J. & Kessler, J.O. 1992 Hydrodynamic phenomena in sus-pensions of swimming microorganisms. *Annu. Rev. Fluid Mech.* **24**, 313–358.

Tuval, I., Cisneros, L., Dombrowski, C., Wolgemuth, C.W., Kessler, J.O. & Goldstein, R.E. 2005 Bacterial swimming and oxygen transport near contact lines. *Proc. Natl Acad. Sci. USA* **102** (7), 2277–2282.